Is the glacial climate scale invariant?

Takahito Mitsui[*,§], Guillaume Lenoir[*], and Michel Crucifix[*,#]

[*]Earth and Life Institute, Georges Lemaître Centre for Earth and Climate Research, Université catholique de Louvain, BE-1348 Louvain-la-Neuve, Belguim

[#]Belgian National Fund of Scientific Research, 1000 Brussels, Belguim

[§]Current address: Atmosphere and Ocean Research Institute, University of Tokyo, Kashiwa, Japan

Correspondence to: Takahito Mitsui (takahito321@gmail.com)

Abstract.

Previous estimates of the power spectrum and of the scaling exponent of the detrended fluctuation analysis of palaeoclimate time series yielded the suggestion that climate fluctuations are scale invariant over a wide range of time scales. The present contribution clarifies the implications of these findings, with focus on the last glacial period. The last glacial period is characterised by Dansgaard-Oeschger events, with rapid and frequent transitions between stadial and interstadial regimes. We therefore consider three simple models known to display regime switching dynamics. Multifractal detrended fluctuation analyses of time series generated by these models reveal that their generalized fluctuation functions have a local scaling regime, with generalized Hurst exponent $h(q)$ being lower for $q \ll 0$ than for $q > 0$. Such dependency of $h(q)$ is qualified here as apparent multifractality. It occurs because the behaviour of the autocorrelation function of small fluctuations (within a regime) differ from that of large fluctuations (regime shifts). It turns out that the generalized Hurst exponent of the oxygen isotope ratio and that of the calcium ion concentration in the NGRIP (Greenland) record exhibit a similar form of apparent multifractality. We then verify that a stochastic model previously used to simulate Dansgaard-Oeschger events, and which also displays regime switching dynamics, generates a generalized Hurst exponent and a power spectrum consistent with the observations. We therefore conclude that the apparent multifractality of these records is a consequence of regime switching between stadial and interstadial climates, and that neither the local scaling in the power spectrum, nor the output of the multifractal detrended fluctuation analysis implies that the underlying process is scale invariant.

1 Introduction

It is a well-known fact of stochastic process theory that uncorrelated fluctuations (i.e. white noises) produce flat power spectra. An accumulation process of such fluctuations under a linear restoring force (the so-called Ornstein-Uhlenbeck (OU) process) yields a Lorentzian spectrum (see Appendix A). Hasselmann (1976) and Frankignoul and Hasselmann (1977) used this element as a basis to elaborate on a theory of climatic fluctuations assuming the existence of a stochastic forcing of the climate system. The stochastic forcing is provided by weather, represented as white noise. The power spectrum of climatic fluctuations then behaves as $P(f) \propto f^{-2}$ in the high-frequency part. Since this pioneering contribution, a number of authors attempted to estimate the power spectra of temperatures at the paleoclimate scale, and they noted enough similarity with the Lorentzian

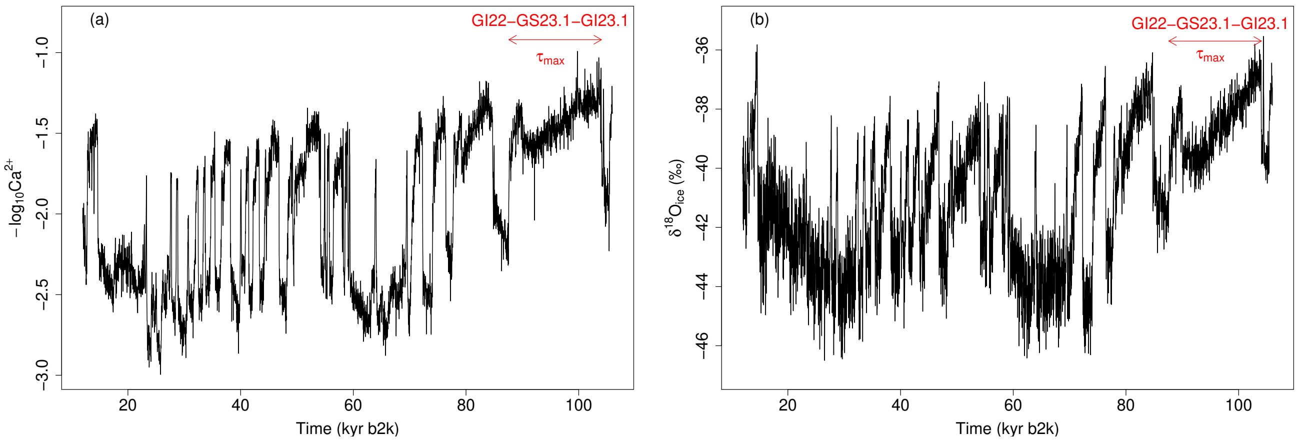

Figure 1. NGRIP ice core records over 12,000–106,000 years b2k (before A.D. 2000): (a) $-\log_{10}[\mathrm{Ca}^{2+}]$ ($[\mathrm{Ca}^{2+}]$ in ppb) and (b) δ^{18}O (Rasmussen et al., 2014). The 20-year averaged values are used in both cases. The arrow shows the longest single regime, GI22–GS23.1–GI23.1 composite, with duration $\tau_{\max} = 16,440$ years, cited in Section 4.

spectrum to suggest that a large part of paleoclimate variations may actually be interpreted as the mere linear accumulation of "weather" noise over tens of millennia (Kominz and Pisias, 1979; Shackleton and Imbrie, 1990; Wunsch, 2003b).

Subsequent analyses of paleoclimate data confirmed that the power spectra of temperatures does indeed follow power laws $P(f) \propto f^{-\beta}$ over wide ranges of frequencies, but the scaling exponent β is generally different from 2 (Pelletier, 1998; Huybers and Curry, 2006; Lovejoy, 2015). These studies also identified several *scaling regimes*, in each of which the exponent β takes a characteristic value, with $0 < \beta < 1$ over the time scale roughly from a month to a century, and $1 < \beta < 2$ over the time scale roughly from a century up to the orbital scale. The value of β depends moderately on the type of proxy (Huybers and Curry, 2006; Lovejoy, 2015).

In this study, we focus on the rapid climate changes called Dansgaard-Oeschger (DO) events (Dansgaard et al., 1993), which constitute the most pronounced mode of centennial-to-millennial-scale climate variability during the glacial periods. While DO signals are most prominent in the North Atlantic region, their imprints are found worldwide (Voelker et al., 2002), including in Antarctica (Barbante et al., 2006; Stocker and Johnsen, 2003).

The DO events were originally identified in Greenland ice core records as abrupt increases in the oxygen isotope ratio δ^{18}O (Fig. 1(b)). The increase which characterizes the onset of a DO event is caused by an upward temperature jump of the order of 8°C up to 16 °C, then followed by a gradual cooling, before a rapid return to the glacial baseline (e.g. Wolff et al. (2010); Rasmussen et al. (2014)). As shown in Fig. 1(a), the logarithm of calcium ion concentration $[\mathrm{Ca}^{2+}]$ (a proxy for dust concentration) is strikingly similar (in fact, anticorrelated) to δ^{18}O (Yiou et al., 1997), and this suggests that DO cycles accompany abrupt changes in atmospheric circulation (Mayewski et al., 1997) and/or changes in dust sources in East Asia (Fischer et al., 2007).

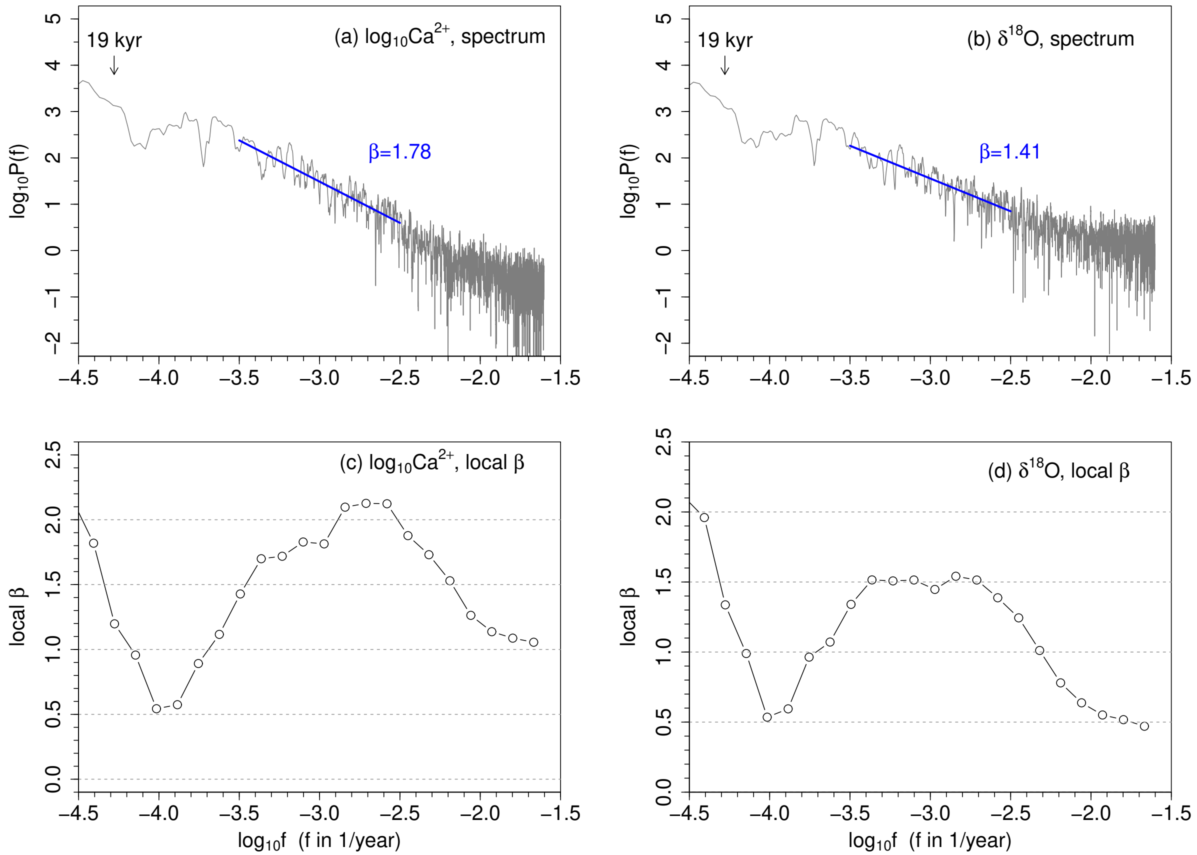

Figure 2. Multitaper method (MTM) power spectral densities (PSD) of (a) NGRIP $\log_{10}$[Ca^{2+}] (gray solid line) and (b) NGRIP δ^{18}O. Both records are standardized as described in Section 4.1 before the spectral analysis. The blue segment shows the scaling law $f^{-\beta}$ in the frequency range $-3.5 < \log_{10} f < -2.5$ (f in 1/yr), where β is estimated by the linear least squares regression of $\log_{10} P(f)$ versus $\log_{10} f$. In MTM, we use the bandwidth parameter $NW = 2$ and three tapers.The upper left arrow indicates one of astronomical frequencies, 19 kyr. (c) and (d) The dependence of the scaling exponent β on the center position of the frequency interval over which β is calculated: (c) the case of $\log_{10}$[Ca^{2+}] and (d) the case of δ^{18}O. The size of the frequency interval for estimating the local β is set to have one order of magnitude.

The log-log plots of the power spectral densities $P(f)$ of the $\log_{10}$[Ca^{2+}] and δ^{18}O records are shown in Figs. 2(a) and 2(b), respectively (see Section 2 for the methods). We estimate the scaling exponent β by linear least squares regression[1] of $\log_{10} P(f)$ on $\log_{10} f$. It is estimated as $\beta = 1.78 \pm 0.04$ (estimate $\pm$ standard error) for $\log_{10}$[Ca^{2+}] and $\beta = 1.41 \pm 0.03$ for δ^{18}O over a frequency interval of $(3162\ \text{yr})^{-1} < f < (316\ \text{yr})^{-1}$ (i.e. $-3.5 < \log_{10} f < -2.5$). The estimate for NGRIP δ^{18}O is consistent with previous estimates $\beta \approx 1.4$ for GRIP δ^{18}O (Schmitt et al., 1995; Ashkenazy et al., 2003; Lovejoy and

[1]The results of two other estimation methods, the binning-based linear regression (Lovejoy and Schertzer, 2012; Fredriksen and Rypdal, 2016) and the Whittle maximum likelihood estimator (Witt and Malamud, 2013), are given in Supplementary material. The following discussion is unaffected by the choice of estimation method.

Schertzer, 2013), for GISP2 δ^{18}O (Rhines and Huybers, 2011), and for NGRIP δ^{18}O (Rypdal and Rypdal, 2016; Shao and Ditlevsen, 2016). It turns out, however, that the value of β largely depends on the position of the frequency interval over which β is estimated (see Figs. 2(c) and 2(d)). This observation is further discussed and explained in Section 4.4.

The Hasselmann's theory of climate spectra does not explain the nontrivial scaling regime with $\beta \neq 2$ observed for the ice core records. We therefore briefly review here a few stochastic processes which may display this property, and which may provide a basis for the interpretation of glacial climate spectra. More comprehensive introductions are available in Lovejoy and Schertzer (2013); Huybers and Curry (2006); Fraedrich et al. (2009); Markonis and Koutsoyiannis (2013); Fredriksen and Rypdal (2017) and references therein.

(i) Time series in the Earth Sciences are often characterized as *self-affine* or more generally *(mono)fractal* (Pelletier and Turcotte, 1999; Witt and Malamud, 2013). The fractional Brownian motion (fBm) with parameter $0 < H < 1$, $B_H(t)$ is a standard model of self-affine time series and defined as a centered Gaussian process with the covariance function $\mathrm{cov}(B_H(s), B_H(t)) = \frac{1}{2}(|s|^{2H} + |t|^{2H} - |t-s|^{2H})$ (Mandelbrot and Van Ness, 1968). The fBm is said to be statistically self-affine because, for any $r > 0$, $\{B_H(rt)\}$ has the same distribution as $\left\{r^H B_H(t)\right\}$. In relation to this self-affinity, the fBm exhibits an $f^{-\beta}$ spectrum with $\beta = 2H + 1$ ($1 < \beta < 3$). The fBm may be understood as an asymptotic limit obtained by aggregating (sum or linear combination of) many OU processes whose time scales and variances follow a geometric progression (i.e. a scale invariance) (Rypdal, 2016; Fredriksen and Rypdal, 2017; Granger, 1980). In practice, the fBm appear to approximate quite well time series generated by linear relaxations systems with no more than four or five of time scales. An example of such a system is the multi-box energy balance model obtained by assembling heat reservoirs representing the atmosphere, the ocean mixed layer and the deep oceans (Fredriksen and Rypdal, 2017). For this reason the fBm is suggested as a plausible process model of climate fluctuations (Nilsen et al., 2014, 2016).

(ii) Another possibility is the *cascade process* (Huybers and Curry, 2006) or, more specifically, the *multifractal cascade process* (Schmitt et al., 1995; Lovejoy and Schertzer, 2013). In fully developed turbulence, kinetic energy is transferred from large scale motions to small scale motions in a self-similar way, creating the so-called energy cascade. Due to the scale-invariance of nonlinear governing equations, the energy spectra follow a power law over the so-called inertial range (e.g., Kolmogolov $k^{-5/3}$ law) (Lovejoy and Schertzer, 2013). Power-law scalings hold also for passive scalar variables such as temperature, and the spatial scalings can be related to the temporal scalings under the assumption that the small-scale turbulent fluctuations are advected by the large-scale velocity (Taylor's frozen hypothesis). Lovejoy and Schertzer (2013) have suggested that the principle of cascade process is also generic to climate phenomena at all time scales, so that scaling regimes are expected throughout the entire climate spectrum. However, because of the nature of the mechanical constraints involved at different spatio-temporal scales, different scaling regimes may emerge (weather, macro-weather, climate), characterized by different scaling exponents. Natural phenomena related to weather such as precipitation and river runoff are well modelled by multifractals cascade processes (Lovejoy and Schertzer, 2013; Koscielny-Bunde et al., 2006; Kantelhardt et al., 2006). While the statistics of a monofractal process like the fBm is characterized by only a single fractal exponent (H), multifractal processes generate an infinite number of fractal exponents. Schmitt et al. (1995) found such a multifractal scaling law in the DO signal of GRIP ice core, which is close to the multifractal scaling law of turbulent atmospheric temperatures observed at weather scales.

(iii) Rypdal and Rypdal (2016) propose an analysis of the DO signal by breaking it down into interstadials, stadials, and abrupt jumps. They pointed out that in each interstadial or stadial, the signal shows an approximate $1/f$ spectrum (i.e. $\beta \approx 1$). The approximate $1/f$ spectrum is then justified as the aggregation of various OU processes (cf. (i) above). However, this decomposition approach does not explain why the power spectrum of the full signal shows a scaling.

At this stage we need to distinguish processes which are inherently scale-invariant, such as the self-affine process and the multifractal cascade process introduced above, from non-scale-invariant processes giving rise to local scaling effects. For example, the OU process presents a local spectral scaling $P(f) \sim f^{-2}$ in the high frequency domain, but the process may not be considered as scale invariant in the sense that its dynamics is governed by a characteristic time scale, the decorrelation time. On the other hand, some processes may have a scale-invariant power spectrum over a reasonably wide range of time scales, but not be fractal nor multifractal. We will refer to this type of scaling as *apparent*. An example is provided by systems switching between distinct regimes, exhibiting a so-called "regime behaviour" (Franzke et al., 2015). Such systems may display a locally scale-invariant spectrum even though the individual regimes do not have any scale invariance property. Examples are given in Section 3. This puzzling fact is well acknowledged in hydrology (Klemeš, 1974; Potter, 1976) or in econometrics (Diebold and Inoue, 2001), but it has not been discussed in the context of DO cycles in the literature as far as we know.

In this study, we show that regime behavior is a consistent explanation for the observed scaling behavior of DO signals. The demonstration makes heavy use of on multifractal analysis. Indeed, while the spectral analysis essentially deals with the second order moment of the fluctuations, the multifractal analysis deals with both higher and lower moments. It therefore provides a more complete characterization of the scaling properties of fluctuations (Lovejoy and Schertzer, 2013; Kantelhardt et al., 2002).

The multifractal properties of Greenland records were previously examined by Schmitt et al. (1995); Marsh and Ditlevsen (1997); Ashkenazy et al. (2003); Lovejoy and Schertzer (2013); Rypdal and Rypdal (2016); Shao and Ditlevsen (2016). They all concluded that the Greenland records of the glacial period are indeed multifractal, except Rypdal and Rypdal (2016), who concluded that they are *mono*fractal. Here we consider simultaneously the multifractal detrended fluctuation analysis and the spectral analysis, and conclude that the underlying process is in fact not scale invariant.

The remainder of this article is organized as follows. In Sect. 2, we explain analysis methods. In Sect. 3, we develop a theory for the apparent multifractality in time series with regime behavior. Sect. 4 presents the analysis of NGRIP ice core records. Sections 5 and 6 are devoted to discussions and conclusion, respectively.

2 Methods

2.1 Multitaper method power spectral density analysis

The adaptive multitaper method (MTM) (Thomson, 1982) averages several periodograms calculated from the same time series. In each periodogram, the original time series is multiplied by a taper function. The MTM reduces the variance of spectral estimates by using a small set of orthogonal tapers rather than the unique data taper or spectral window used by classical methods (Harris, 1978). The number of tapers, K, determines the frequency resolution and variance of the estimates. For the

MTM or any other spectral estimator, there is always a trade-off between increasing the frequency resolution and reducing the variance. Usually, K is selected to be less than $2NW-1$, where NW is the so-called bandwidth parameter, typically between 2 and 6. Fortunately, our conclusions are robust against tapering. For instance, the MTM and the periodogram without tapering give almost the same results (compare Fig. 2 and Supplementary Fig. 1). Here, two-sided MTM power spectral densities (PSD) were estimated with the function `spec.mtm` in the R-package 'Multitaper' (Rahim and Burr, 2013).

2.2 Multifractal detrended fluctuation analysis (MF-DFA)

The detrended fuctuation analysis (DFA) is a method for the determination of monofractal scaling properties and the detection of long-range correlations in nonstationary time series (Peng et al., 1994). It was applied to long temperature observations (Koscielny-Bunde et al., 1998; Fraedrich and Blender, 2003), past temperature reconstructions (Ashkenazy et al., 2003; Rybski et al., 2006) as well as climate model simulations (Fraedrich and Blender, 2003).

The multifractal detrended fluctuation analysis (MF-DFA) is a generalization of the DFA (Kantelhardt et al., 2002). Suppose that x_k is the time series of length N and of compact support, i.e., $x_k = 0$ only for an insignificant fraction of the series. In MF-DFA, the cumulated series, called the profile, $Y(i) = \sum_{k=1}^{i}(x_k - \langle x \rangle)$ is constructed from the original time series x_k with mean $\langle x \rangle$. This profile is then split into $N_s \equiv \lfloor N/s \rfloor$ non-overlapping segments of size s. Since N is not always a multiple of s, a short part may remain at the end of the profile. In order to count this part, the same procedure is repeated from the opposite end. Hence, a total of $2N_s$ segments are obtained. In each segment indexed by ν, a local trend of the profile is estimated with a polynomial fit $y_\nu(i)$. Then, one calculates the variance of the detrended profile $F^2(\nu,s) = \frac{1}{s}\sum_{i=1}^{s}\{Y[(\nu-1)s+i] - y_\nu(i)\}^2$ for segments $\nu = 1,...,N_s$ and $F^2(\nu,s) = \frac{1}{s}\sum_{i=1}^{s}\{Y[N-(\nu-1)s+i] - y_\nu(i)\}^2$ for segments $\nu = N_s+1,...,2N_s$. In the m-th order of MF-DFA (MF-DFAm), local trends of order m in the profile are eliminated (this is equivalent to eliminating local trends of order $m-1$ in the original record). A comparison of the results for different orders of MF-DFA allows one to estimate the type of the polynomial trend in the time series (Kantelhardt et al., 2002). The generalized fluctuation function for $q \neq 0$ is calculated as:

$$F_q(s) \equiv \left\{ \frac{1}{2N_s} \sum_{\nu=1}^{2N_s} [F^2(\nu,s)]^{q/2} \right\}^{1/q}. \tag{1}$$

When $q = 0$, logarithmic averaging is applied:

$$F_0(s) \equiv \exp\left\{ \frac{1}{4N_s} \sum_{\nu=1}^{2N_s} \ln[F^2(\nu,s)] \right\}. \tag{2}$$

For a scaling process, the generalized fluctuation function scales as

$$F_q(s) \sim s^{h(q)},$$

where $h(q)$ is called the *generalized Hurst exponent* (Kantelhardt et al., 2002) and is estimated from the log-log plot of $F_q(s)$. For very large scales $s > N/4$, the values of $F_q(s)$ are statistically unreliable since the number of samples is small, and for

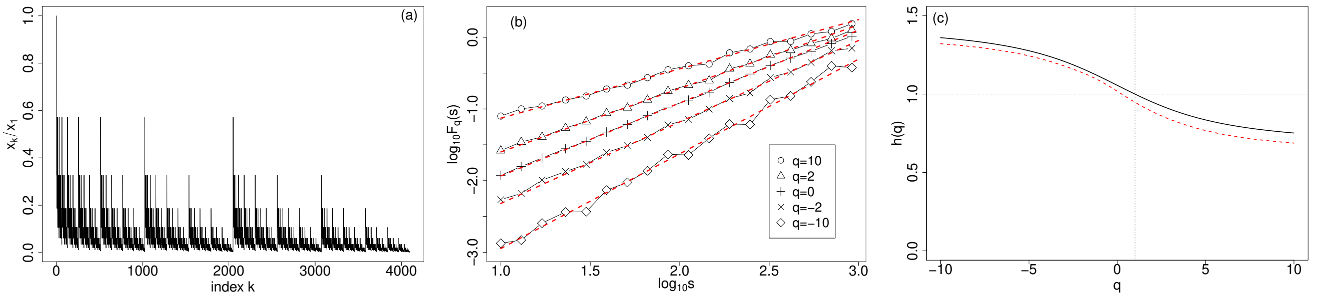

Figure 3. Multifractal detrended fluctuation analysis of the binomial multiplicative cascade model: (a) A series of the binomial multiplicative cascade model with parameter $a = 0.7$ and $b = 0.4$. In this model, the series of length $N = 2^{n_{\max}} = 4096$ ($n_{\max} = 12$) is recursively constructed. In the 0-th generation, $x_k = 1$ for all k. In the first step, the first half of the series is multiplied by a factor a and the second half by a factor b ($0 < b < a < 1$). This yields the 1st generation: $x_k = a$ for $k = 1, ..., N/2$ and $x_k = b$ for $k = N/2+1, ..., N$. In the second step, the same process is applied to the two subseries, which gives the second generation $x_k = a^2$ for $k = 1, ..., N/4$, $x_k = ab = ba$ for $k = N/4+1, ..., 3N/4$ and $x_k = b^2$ for $k = 3N/4+1, ..., N$. This cascade process is repeated recursively and, at the n-th generation, the series is given as $x_k = a^{n_{\max}-n(k-1)} b^{n(k-1)}$, where $n(k)$ is the number of the digits 1 in the binary representation of the index k. (b) Generalized fluctuation function $F_q(s)$ for x_k/x_1. The red dashed lines are the best-fitting lines, whose slopes are estimated by the linear least squares regression over $50 < s < 500$. (c) The generalized Hurst exponent for the binomial cascade model: The theoretical curve (black) is given by $h(q) = \frac{1}{q} - \frac{\ln(a^q + b^q)}{q \ln 2} + \frac{\ln(a+b)}{\ln 2}$, which passes $(1, 1)$, the intersection of vertical and horizontal dotted lines (Kantelhardt, 2009). The red dashed line is numerically obtained by the fitting to $F_q(s)$ shown in (b). The difference between the theoretical curve and the one obtained numerically is less than 0.07 over $-10 < q < 10$.

very small scales $s < 10$, systematic deviations from the scaling behavior occur (Kantelhardt et al., 2002). Hence, these scales are excluded from the analysis.

For $q = 2$, MF-DFAm reduces to the conventional DFAm, and the scaling exponent $h(2)$ is related to the scaling exponent β of the power spectrum (Heneghan and McDarby, 2000):

$$\beta = 2h(2) - 1 \ \text{ or } \ h(2) = (\beta + 1)/2. \tag{3}$$

For reference, the white Gaussian noise has a flat spectrum with $\beta = 0$ and hence $h(2) = 0.5$; the Brownian motion has the scaling spectrum $\propto f^{-2}$ (i.e. $\beta = 2$) and hence $h(2) = 1.5$. The fluctuation function $F_2(s)$ of an AR(1) process (autoregressive process of order 1, which may be seen as the discrete form of an OU process) is available in a closed form in Höll and Kantz (2015). The exponent $h(2)$ of an AR(1) process is $h(2) = 0.5$ for long time scales, and approximates to $h(2) \approx 1.5$ for short time scales.

A scaling process is said to be *monofractal* if $h(q)$ is independent of q. For instance, the Brownian motion is monofractal: $h(q) = h(2) = 1.5$ (Kantelhardt et al., 2002). A scaling process is said to be *multifractal* when $h(q)$ depends on q. Equation (1) implies that $F_q(s)$ is dominated by large fluctuations when q is positive, and by small fluctuations when q is negative. Thus, $h(q)$ for $q > 0$ describes the scaling properties of the segments with large fluctuations. Conversely, $h(q)$ for $q < 0$ describes the scaling properties of the segments with small fluctuations.

Typically the generalized Hurst exponent $h(q)$ monotonically decreases as q increases. This is understood as follows: Since $F_q(s)$ is the generalized mean of the local standard deviations $F^2(\nu,s)^{1/2}$, the generalized mean inequality holds, that is, for $s < N$, $F_q(s) \leq F_{q'}(s)$ if $q \leq q'$ (e.g. Fig. 3(b)). On the other hand, at the maximum scale $s = N$, the generalized fluctuation function $F_q(s)$ becomes independent of q since the sum in Eq. (1) runs over only two identical segments. In other words, all the graphs of functions $F_q(s)$ with different q are pinched at $s = N$. Therefore, if we assume a homogeneous scaling behavior of $F_q(s) \sim s^{h(q)}$ over the entire time scale, the slope $h(q)$ in the log-log plot of $F_q(s)$ should be smaller or equal for large q than for small q (e.g. Fig. 3(b)), making $h(q)$ monotonically decreasing for increasing q (e.g. Fig. 3(c)). This behaviour is indeed verified in known examples of natural multifractal behavior (Koscielny-Bunde et al., 2006; Kantelhardt et al., 2006) as well as in classical multitifractal models (Kantelhardt et al., 2002; Kantelhardt, 2009). Figure 3 shows an example of such a truly multifractal model, the binomial multiplicative cascade model (see caption for details), whose generalized Hurst exponent $h(q)$ is monotonically decreasing (Fig. 3(c)). A significant violation of the monotonically-decreasing property of $h(q)$ may imply the invalidity of the homogeneous scaling assumption. Ludescher et al. (2011) show that periodicities like seasonal trends added to multifractal or even monofractal time series can yield untypical, increasing generalized Hurst exponents. Such a phenomenon is called “spurious reversed multifractality”.

There are mainly two types of multifractality of time series (Kantelhardt et al., 2002): (i) the multifractality resulting from different long-range autocorrelations of the small and large fluctuations and (ii) the multifractality resulting from a heavy-tailed probability density function of the values of time series. The first type of multifractality is destroyed by randomly shuffling the time series because autocorrelations are then lost. The generalized Hurst exponent $h(q)$ is then simply 0.5. The same operation will not affect multifractality in the second case.

3 Apparent multifractality that is characteristic of regime switching patterns

Before analyzing Greenland records in the next section, we study a few classical dynamical system models to characterize a form of apparent multifractality specific to a regime behavior. In MF-DFA, we use quadratic polynomial detrending (MF-DFA2) unless otherwise mentioned.

3.1 Random telegraph process with additive white Gaussian noise

The random telegraph process $x(t)$ takes one of two states: $x(t) = a$ and $x(t) = c$. When $x(t) = a$, the transition $a \to c$ occurs in $(t, t+dt)$ with probability λdt, and the waiting time τ until the next transition is given by an exponential probability density $\lambda e^{-\lambda\tau}$. When $x(t) = c$, the transition $c \to a$ occurs in $(t, t+dt)$ with a probability density μdt. We define the signal $y(t) = x(t) + \xi(t)$, where $\xi(t)$ is an independent white Gaussian noise with variance σ^2. This additional noise $\xi(t)$ can be interpreted as a representation of observation errors, as they occur in real-world experiments, or as an expression of fast, non-cumulative atmospheric fluctuations. In what follows, we use $a = -1$, $c = 1$, $\lambda = \mu = 0.01$, and $\sigma^2 = 0.01$, and analyze a time series of $y(t)$ sampled at $t = s\Delta t$ ($s = 1, ..., N$) with $\Delta t = 1$ (see Fig. 4(a)).

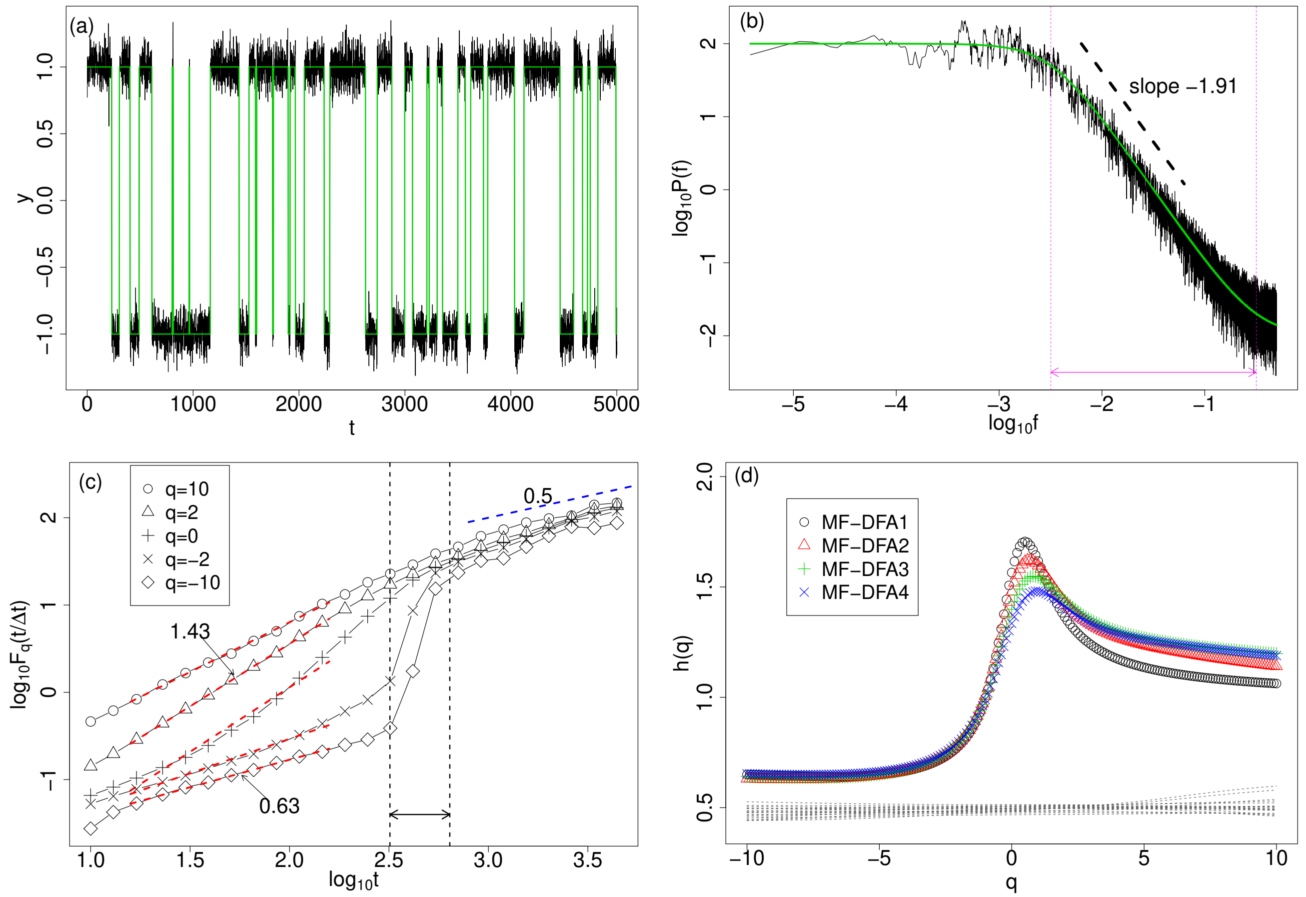

Figure 4. Analysis of the random telegraph process with additive white Gaussian noise. $a = -1$, $c = 1$, $\lambda = \mu = 0.01$, and $\sigma^2 = 0.01$. (a) A sample time series of the random telegraph process $x(t)$ (green line) and that with additive white Gaussian noise $y(t) = x(t) + \xi(t)$ (black line). Both are sampled at $t = s\Delta t$ ($s = 1, 2, ...;\ \Delta t = 1$). The first 5000 points are presented. (b) MTM power spectral density (PSD) of $y(t) = x(t) + \xi(t)$ sampled at $t = s\Delta t$ ($s = 1, 2, ..., 10^6;\ \Delta t = 1$) is shown by the black line. The bandwidth parameter is $NW = 4$, and the number of tapers is $K = 7$. The green line shows the theoretical PSD, which roughly scales as $P(f) \sim f^{-2}$ in the frequency range $f_1 \ll f \ll f_2$ indicated by the magenta arrow (see text for f_1 and f_2). (c) MF-DFA2 generalized fluctuation function $F_q(t/\Delta t)$ for $y(t)$ sampled at $t = s\Delta t$ ($s = 1, 2, ..., 20000;\ \Delta t = 1$). The red dashed lines indicate scaling laws over $1.2 < \log_{10} t < 2.2$ corresponding to the frequency range $f_1 < f < f_2$. The function $F_q(t/\Delta t)$ for $q \ll 0$ sharply increases in the time range $\frac{\tau_{\max}}{2} < t < \tau_{\max}$ indicated by the black arrow, where $\tau_{\max} = 639$ is the maximum duration of a single regime in the analyzed time series. (d) Generalized Hurst exponent $h(q)$ obtained by the fitting over $1.2 < \log_{10} t < 2.2$. Each symbol corresponds to a different order, m, of detrending in the MF-DFAm. The gray dashed lines show the exponents $h(q)$ for 20 randomly shuffled data, which are obtained by the fitting over $1.5 < \log_{10} t < 2.5$.

The power spectral density (PSD) of the process $y(t)$ can be determined analytically. The random telegraph process $x(t)$ has an exponentially decaying autocovariance $\rho(\tau) = \frac{(a-c)^2\lambda\mu}{(\lambda+\mu)^2} e^{-(\lambda+\mu)|\tau|}$ (Gardiner (2009), p. 75). By using the Wiener-Khinchin theorem, we find that the PSD is a Lorentzian:

$$P_x(f) = \frac{2\lambda\mu(a-c)^2}{\lambda+\mu}\frac{1}{(\lambda+\mu)^2+(2\pi f)^2}. \tag{4}$$

Since the PSD of the white Gaussian noise $\xi(t)$ is $P_\xi(f) = \sigma^2$ and since $x(t)$ and $\xi(t)$ are independent, the PSD of $y(t)$ is the sum $P(f) = P_x(f) + P_\xi(f)$ (Fig. 4(b)). From the analytical form of $P(f)$, we may expect the following scaling behavior[2]: $P(f) \sim f^{-2}$ for $f_1 \ll f \ll f_2$ and $P(f) \sim$ const. for $f \ll f_1$ and $f \gg f_2$, where $f_1 \equiv \frac{\lambda+\mu}{2\pi}$ and $f_2 \equiv \frac{1}{2\pi}\sqrt{\frac{2\lambda\mu(a-c)^2}{(\lambda+\mu)\sigma^2} - (\lambda+\mu)^2}$. Indeed, we numerically obtain $\beta = 1.91 \pm 0.005$ over $-2.2 < \log_{10} f < -1.2$ (Fig. 4(b)).

We then analyze the process $y(t)$ with MF-DFA2. The result is qualitatively robust against the order of the detrending, but sensitivity to the order of detrending is discussed at the end of this subsection. Figure 4(c) shows the log-log plot of the MF-DFA2 generalized fluctuation function $F_q(t/\Delta t)$ for $y(t)$, where $F_q(s)$ in Eqs. (1) and (2) is transformed to $F_q(t/\Delta t)$ via $t = s\Delta t$. A local multifractal scaling law seems to emerge at relatively short time scales, around $1.2 < \log_{10} t < 2.2$, but $F_q(t/\Delta t)$ is no longer scaling near $q = 0$. The behavior of F_q then indicates monofractal scaling at the limit of long time scales ($\log_{10} t > 3$), with exponent $h(q) = 0.5$ as in the white Gaussian noise. The fluctuation function $F_2(t/\Delta t)$ for $q = 2$ (triangles in Fig. 4(c)) is related to the PSD: The generalized Hurst exponent $h(2) = 1.43 \pm 0.01$ for $f_2^{-1} < t < f_1^{-1}$ is consistent with the scaling exponent $\beta = 1.91 \pm 0.005$ for $f_1 < f < f_2$ via Eq. (3). Also, the generalized Hurst exponent $h(2) \approx 0.5$ for longer $t \gg f_1^{-1}$ is consistent with the scaling exponent $\beta = 0$ for $f \ll f_1$.

The scaling behavior of the generalized fluctuation function $F_q(t/\Delta t)$ depends on the duration of the largest single regime found in the time series. In our example (Fig. 4(a)), this duration, called $\tau_{\max}$, is 639 ($\log_{10}\tau_{\max} = 2.8$). We find that $F_q(t/\Delta t)$ for $q \ll 0$ sharply increases in the range

$$\frac{\tau_{\max}}{2} < t < \tau_{\max}.$$

We explain this phenomenon as follows: (i) When the segment size t is less than $\frac{\tau_{\max}}{2}$, there must be segments with no regime shift. These segments contain only white Gaussian noises and have smaller variances. Since the generalized fluctuation function $F_q(s)$ for $q \ll 0$ is dominated by the variances of small fluctuations (here white Gaussian noises), the generalized Hurst exponent $h(q)$ for $q \ll 0$ is expected to take a value close to 0.5 corresponding to white Gaussian noise. Indeed, we numerically obtain $h(q) \approx 0.6$ for $q \ll 0$ (the difference 0.1 from the expected value 0.5 is thought to be the contribution of the segments with regime shifts). (ii) When the segment size t is greater than $\tau_{\max}$, all the segments have at least one regime shift. Thus, the contrast between segments with and without regime shifts, which induced q-dependence for $t \lesssim \frac{\tau_{\max}}{2}$, vanishes, and hence $h(q)$ tends to $h(2) = 0.5$ for $t \gg \tau_{\max} (> f_1^{-1})$.

The generalized Hurst exponent $h(q)$ is qualitatively independent of the order of the detrending, m, as shown in Fig. 4(d). Nevertheless, there is a non-negligible difference in $h(q)$ between MF-DFA1 and higher-order MF-DFAm's because only the MF-DFA1 does not remove the trend in the original record. For randomly shuffled data, we obtain monofractal scaling with $h(q)$ close to 0.5, as shown by gray dashed lines in Fig. 4(d). This result confirms that the apparent multifractality is caused

[2]The derivation of the scaling behavior is straightforward. For example, $P(f) = \frac{2\lambda\mu(a-c)^2}{\lambda+\mu}\frac{1}{(\lambda+\mu)^2+(2\pi f)^2} + \sigma^2$ scales as f^{-2} if the first term in the right hand side is much greater than the second term σ^2 and if the term $(2\pi f)^2$ in the denominator is much greater than $(\lambda+\mu)^2$. This gives the scaling range $f_1 \ll f \ll f_2$.

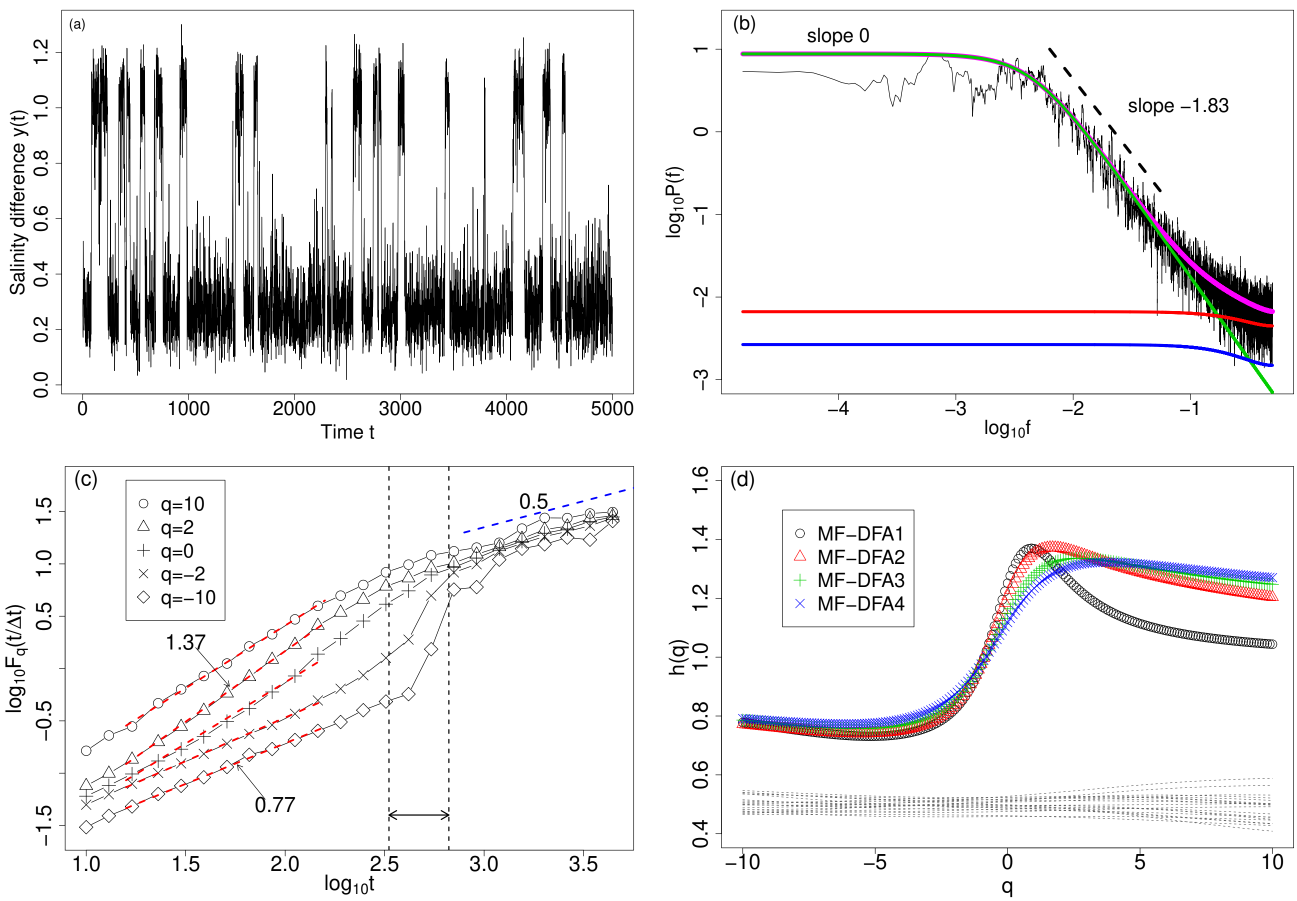

Figure 5. Analysis of the Stommel-Cessi model. (a) A time series of $y(t)$ sampled at $t = s\Delta t$ ($s = 1, 2, ...; \Delta t = 1$). The first 5000 points are presented. (b) MTM power spectral density (PSD) of $y(t)$ sampled at $t = s\Delta t$ ($s = 1, 2, ..., 20000; \Delta t = 1$) (black line). The bandwidth parameter is $NW = 4$, and the number of tapers is $K = 7$. The slope -1.82 is obtained over $-2.2 < \log_{10} f < -1.2$. The thick magenta line is the theoretical approximation of the PSD $P(f) = P_1(f) + P_2(f) + P_3(f)$, which consists of the Lorentzian $P_1(f)$ (green) and two AR(1) PSDs $P_2(f)$ (red) and $P_3(f)$ (blue). (c) MF-DFA2 generalized fluctuation function $F_q(t/\Delta t)$ for $y(t)$ sampled at $t = s\Delta t$ ($s = 1, 2, ..., 20000; \Delta t = 1$). The scaling behavior changes drastically in the time range $\frac{\tau_{\max}}{2} < t < \tau_{\max}$ shown by the arrow, where $\tau_{\max} = 665$ is the maximum duration of a single regime. (d) Generalized Hurst exponent $h(q)$ obtained by the fitting over $1.2 < \log_{10} t < 2.2$. Each symbol corresponds to a different order, m, of detrending in the MF-DFAm. The gray dashed lines show the exponents $h(q)$ for 20 randomly shuffled data obtained by the fitting $F_q(t/\Delta t)$ over $2 < \log_{10} t < 3$.

by different autocorrelations of the small fluctuations (uncorrelated noises) and large fluctuations (regime shifts with longer correlation time $\frac{1}{\lambda+\mu} = 50$).

3.2 Stommel-Cessi's box model of thermohaline circulation

Variations in the thermohaline circulation are considered to have large impacts on climate (Rahmstorf, 2002). Stommel (1961) presented a model of thermohaline circulation consisting of two interconnected boxes. Due to the nonlinear advection feedback of salt and heat, the model can have bistable circulation modes. Cessi (1994) analyzed the Stommel model under stochastic freshwater forcings and discussed the relation with abrupt climate changes. A simplified version of the Stommel-Cessi model is obtained in the form of a stochastic differential equation for the non-dimensional salinity gradient y:

$$\frac{dy}{dt} = -[1+\mu^2(y-1)^2]y + \overline{p} + p'(t),$$

where we use $\mu^2 = 6.2$, $\overline{p} = 1.1$, and $p'(t)$ is the white Gaussian noise with variance $\sigma^2 = 0.033$. The system can be written with the potential function $V(y) = \mu^2\left(\frac{1}{4}y^4 - \frac{2}{3}y^3 + \frac{1}{2}y^2\right) + \frac{1}{2}y^2 - \overline{p}y$ as $\frac{dy}{dt} = -\frac{\partial V(y)}{\partial y} + p'(t)$. For the above parameter values, $V(y)$ is a double well potential. The trajectories spend most of the time in the neighborhood of two potential minima $y_a \approx 0.24$ and $y_c \approx 1.07$, and exhibit random regime-switching in between two wells by jumping over the potential barrier as shown in Fig. 5(a).

Cessi (1994) shows that the PSD of $y(t)$ is well approximated by the sum of three Lorentzian spectra $P(f) = P_1(f) + P_2(f) + P_3(f)$: $P_1(f)$ is a Lorentzian corresponding to random telegraphic jumps between minimums of potential. $P_2(f)$ and $P_3(f)$ are Lorentzians corresponding to linearized equations around each minimum, namely OU processes, respectively. If the process is sampled at regular time intervals, then P_2 and P_3 need to be replaced by the spectra of AR(1) processes. Explicit forms for P_1, P_2 and P_3 are given in Appendix B. In Fig. 5(b) we can see that the approximate PSD, $P(f)$, matches well with the PSD of a simulated time series $y(t)$. In other words, the time series generated by the stochastic box-model is approximately the sum of the random telegraphic jumps and AR(1) processes around each potential minimum. While the Lorentzian spectrum asymptotically scales as $f^{-\beta}$ ($\beta = 2$) as $f \to \infty$, the scaling exponent β of $P(f)$ is less than 2 because of the crossover from $\beta = 2$ to 0 as f decreases (relaxation effect), and also because the AR(1) spectrum flattens at high frequencies (discretization effect).

We analyze the signal $y(t)$ sampled at $t = s\Delta t$ ($s = 1, 2, ...; \Delta t = 1$) with the MF-DFA2. Again, sensitivity to the order of detrending will be discussed later. Figure 5(c) shows the log-log plot of the MF-DFA2 generalized fluctuation function $F_q(t/\Delta t)$ for $y(t)$. A local multifractal scaling law appears at relatively short time scales, around $1.2 < \log_{10} t < 2.2$. The deviation from the scaling law near $q = 0$ is less conspicuous than in the random telegraph model. At long time scales ($\log_{10} t > 3$), there is monofractal scaling with exponent $h(q) \approx 0.5$. The exponent $h(2) = 1.37 \pm 0.01$ over $1.2 < \log_{10} t < 2.2$ is consistent with the spectral scaling exponent $\beta = 1.83 \pm 0.01$ for the corresponding frequency interval, via Eq. (3). The exponent $h(2) \approx 0.5$ for large t is also consistent with $\beta = 0$ for small f.

The scaling behavior of the generalized fluctuation function $F_q(t/\Delta t)$ depends again on the maximum duration of a single regime, $\tau_{\max}$ in the time series [$\tau_{\max} = 665$ ($\log_{10} \tau_{\max} = 2.8$) in the sample series in Fig. 5(a)]. The scaling behavior of $F_q(t/\Delta t)$ changes in the range $\frac{\tau_{\max}}{2} < t < \tau_{\max}$ accompanied with prominent increases for $q \ll 0$. When the segment size t is less than $\frac{\tau_{\max}}{2}$, we have segments without regime shifts. The fluctuations in these segments are approximately AR(1) processes, which have smaller variances compared to regime shifts. Since the generalized fluctuation function $F_q(s)$ for $q \ll 0$ is weighted by small fluctuations, we may expect $h(q) = 0.5$ for $q \ll 0$ corresponding to the asymptotic character of the AR(1) processes. In the simulation, we obtain $h(q) = 0.77$ for $q = -10$, which is substantially larger than 0.5. We interpret this difference as an effect of short-range correlation in AR(1) processes, already found by Ludescher et al. (2011).

While the shape of the generalized Hurst exponent $h(q)$ is qualitatively independent of the order m of detrending (Fig. 5(d)), there is a non-negligible difference between MF-DFA1 and higher-order MF-DFAm's ($m \geq 2$) for large positive q. For randomly shuffled data, we obtain monofractal scaling with $h(q) = 0.5$, as shown by gray dashed lines in Fig. 5(d), and this confirms that the apparent multifractality is caused by the difference between the autocorrelations of small fluctuations (AR(1) processes) and that of large fluctuations (regime shifts).

3.3 Short summary of the model analyses

Regime behavior yields relative long, but finite-time, autocorrelations, which induce apparent scalings in power spectra and in generalized fluctuation functions. The scaling behavior in the generalized fluctuation function $F_q(t/\Delta t)$ changes drastically in the time range $\frac{\tau_{\max}}{2} < t < \tau_{\max}$, where $\tau_{\max}$ is the maximum duration of a single regime in the analyzed time series. The generalized Hurst exponent $h(q)$ obtained for time scales $t < \frac{\tau_{\max}}{2}$ has smaller values for $q \ll 0$ than for $q > 0$ because the autocorrelation function associated with small fluctuations (fluctuations in each regime) differs from that of large fluctuations (regime shifts). The generalized Hurst exponent $h(q)$ tends to have a canonical value of 0.5 for time scales $t > \tau_{\max}$.

The dependence of $h(q)$ found in the previous two models is also found in the classical Lorenz (1963) model (see Appendix C). As Franzke et al. (2015) pointed out, the chaotic motion in the Lorenz attractor may indeed be interpreted as a regime behavior. Hence, we suggest that apparent multifractality with the specific form of $h(q)$ documented above is a signature of regime behavior.

4 Apparent scaling in Dansgaard-Oeschger cycles

4.1 NGRIP ice core records

We analyze the 20-year average NGRIP $\log_{10}$[Ca^{2+}] and δ^{18}O records[3] during 12–106 kyr b2k, already shown in Figs. 1(a) and 1(b) (Rasmussen et al., 2014). These DO signals may be interpreted as regime behavior between stadials and interstadials. In the previous section, we mentioned that the maximum duration of a single regime is important for characterizing the behavior of the generalized fluctuation function. In these records, defining a single regime is not a simple task. A slightly cooler period 90,040–90,140 yr b2k is referred to as a Greenland Stadial (GS23.1) by Rasmussen et al. (2014). However the same authors consider GS23.1 as probably part of an interstadial since it is short, and the Ca^{2+} record, in particular, does not reach stadial values. Hence we also assume GI22–GS23.1–GI23.1 as a single regime, which has the longest duration of $\tau_{\max} = 16,440$ years. In what follows, we use the proxy records standardized by their mean and standard deviation during 11–100 kyr BP: $y(t) = (-\log_{10}[\mathrm{Ca}^{2+}] + 2.02)/0.464$ and $y(t) = (\delta^{18}\mathrm{O} + 41.155)/2.236$.

[3]The 20-year average NGRIP [Ca^{2+}] record provided in Seierstad et al. (2014) has 18 missing values during 12–106 kyr b2k, which represent 0.4% of the 4701 data points. As this number of missing data is very small, we filled the gaps by linear interpolation for simplicity

Table 1. Parameter values of the stochastic dynamical system model for two proxy records taken from the NGRIP ice core. The parameter set for $\log_{10}[\mathrm{Ca}^{2+}]$ is the maximum likelihood estimator obtained in Mitsui and Crucifix (2017). The parameter set for δ^{18}O is estimated with the same approach, but we choose a parameter set corresponding to a local maximum of the likelihood function because it is more consistent with the parameter set for $\log_{10}[\mathrm{Ca}^{2+}]$.

Proxy	k	x_*	α	β	σ_1	σ_2	ε	γ_0	γ_1	γ_2
$\log_{10}[\mathrm{Ca}^{2+}]$	38	-0.081	-0.32	58	1.3	0.78	0.074	-0.15	0.34	0.57
δ^{18}O	28	-0.18	3.4	24	1.9	0.68	0.264	-0.12	0.34	0.55

4.2 Stochastic dynamical system (SDS) model

Extending the model in Kwasniok (2013), Mitsui and Crucifix (2017) model each proxy record $y(t)$ as a noisy observation of a climate variable $x(t)$ represented by a forced stochastic oscillator:

$$dx(t) = \left\{kv - \alpha x - \frac{\beta}{3}[(x-x_*)^3 + x_*^3]\right\} dt + \sigma_1 dW_1(t), \tag{5}$$

$$dv(t) = \{-x + \gamma_0 + \gamma_1 I(t) - \gamma_2 V(t)\}\, dt + \sigma_2 dW_2(t), \tag{6}$$

$$y(t) = x(t) + \eta(t),$$

where t is the time in kyr, $v(t)$ is a hidden variable enabling oscillatory behavior, $W_1(t)$ and $W_2(t)$ are mutually independent Wiener processes, $I(t)$ is the summer solstice daily-mean insolation at 65°N (Laskar et al., 2004), and $V(t)$ is the global ice volume (see below). The observation noise $\eta(t)$ is supposed to capture all the discrepancies between the climate state and the observed proxy value, and it is simply modeled by a white Gaussian noise with variance ε^2. Mitsui and Crucifix (2017) used a benthic δ^{18}O stack record (Lisiecki and Raymo, 2005) for the approximate global ice volume $V(t)$. Here it is simulated with the conceptual model of Paillard (1998) to show that the nontrivial spectral scaling is indeed simulated, rather than imposed by the forcing. The ice volume is simulated as shown in Fig. 4 of his paper and input into $V(t)$ of Eq. (6) but scaled so as to have mean -0.078 and standard deviation 1.013, which are those of the forcing used in Mitsui and Crucifix (2017) over 12–107 kyr BP. The values of the model parameters are given in Table 1. Sample trajectories simulated by this model are shown in Supplementary Fig. 3.

4.3 MF-DFA of DO signals

First, we evaluate an appropriate order of detrending, m, used in the MF-DFAm. Figures 6(a–d) show the generalized fluctuation functions $F_q(t/\Delta t)$ for $\log_{10}[\mathrm{Ca}^{2+}]$ and δ^{18}O in cases of $q = 2$ and $q = -2$, respectively. The unit of t is year and the sampling interval is $\Delta t = 20$ year in this section. While the slopes calculated over $3.0 < \log_{10} t < 3.9$ in higher-order MF-DFAm's are similar, the slope in MF-DFA1 is rather different from the others, especially when q is negative. This is because only the MF-DFA1 fails in removing the trend in the original DO signals. Given the clear trends in DO signals caused by

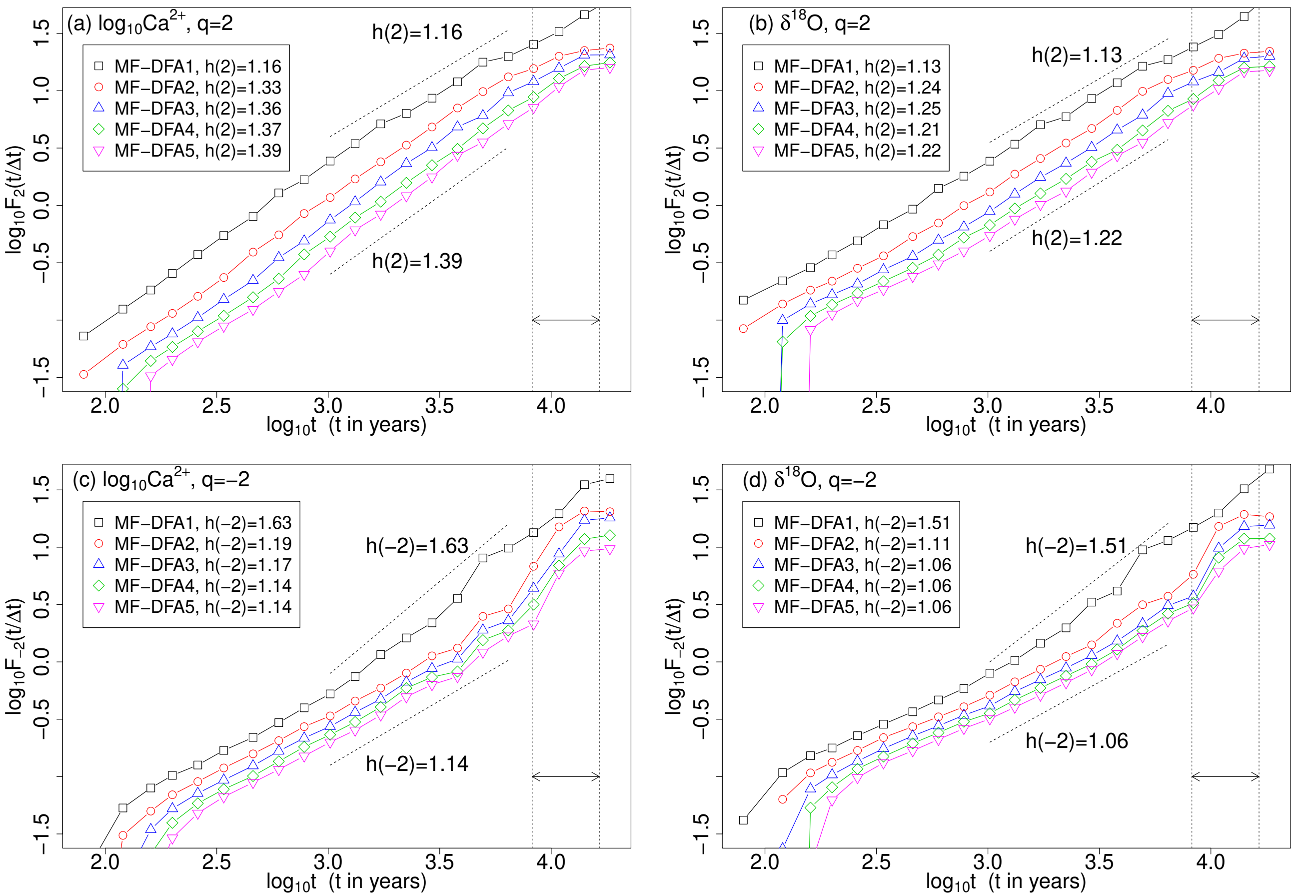

Figure 6. Dependence of MF-DFAm on the order of detrending, m: The generalized fluctuation functions for (a) NGRIP $\log_{10}$[Ca^{2+}] record and $q = 2$, (b) NGRIP δ^{18}O record and $q = 2$, (c) $\log_{10}$[Ca^{2+}] and $q = -2$, and (d) δ^{18}O and $q = -2$. The slopes over $3.0 < \log_{10} t < 3.9$ are shown in the legend. In MF-DFAm ($m \geq 2$), the scaling behavior changes drastically in the range $\frac{\tau_{\max}}{2} < t < \tau_{\max}$ indicated by the arrow, where $\tau_{\max} = 16,440$ years is the maximum duration of a single regime. Some of the slope values cited in the text are indicated.

the long-term glacial-interglacial cycles, we henceforth focus on the results of MF-DFA2. However, the conclusion does not depend on the the order of the detrending except that the crossover time scale is different between MF-DFA1 and higher-order MF-DFAm's.

Figures 7(a) and 7(b) show the generalized fluctuation functions $F_q(t/\Delta t)$ for $\log_{10}$[Ca^{2+}] and δ^{18}O, respectively. We find a local multifractal scaling over a multicentennial-to-multimillennial range. The scaling behavior changes drastically in $\frac{\tau_{\max}}{2} < t < \tau_{\max}$ (i.e. $8220 < t < 16440$ yr). First, we compute the generalized Hurst exponent $h(q)$ by fitting $F_q(t/\Delta t)$ over a multicentennial-to-multimillennial range $2.5 < \log_{10} t < 3.5$ (i.e. $316 < t < 3162$ yr). The resultant generalized Hurst exponents $h(q)$ are unimodal and have lower values for $q \ll 0$ than for $q > 0$, as shown in Figs. 8(a) and 8(b). When the data are randomly shuffled, the generalized Hurst exponent $h(q)$ becomes independent of q as shown by gray dashed lines. These

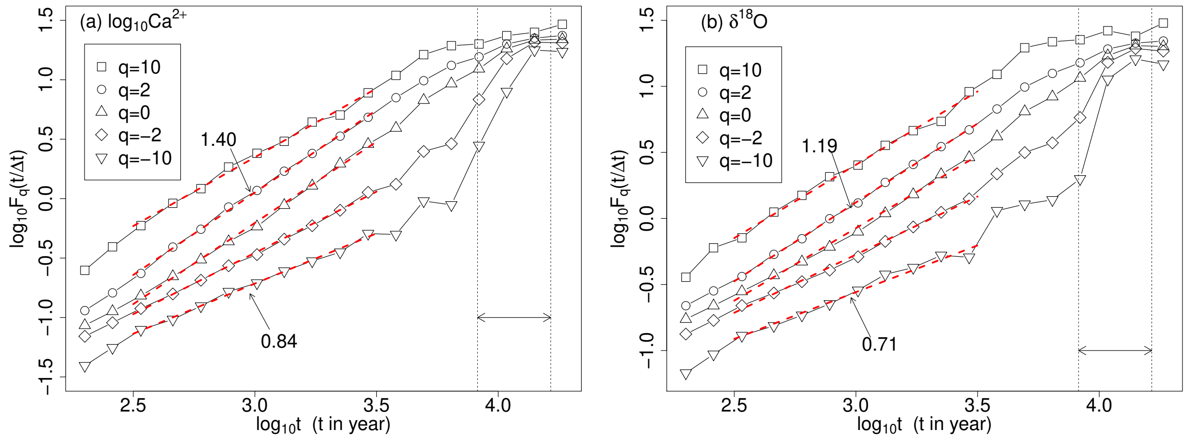

Figure 7. MF-DFA2 generalized fluctuation functions $F_q(t/\Delta t)$ for (a) NGRIP $\log_{10}[\mathrm{Ca}^{2+}]$ record and (b) NGRIP δ^{18}O record. The functions $F_q(t/\Delta t)$ are shown by different points depending on the value of q. The scaling behavior changes drastically in the range $\frac{\tau_{\max}}{2} < t < \tau_{\max}$ indicated by the arrow, where $\tau_{\max} = 16,440$ years is the maximum duration of a single regime. The red dashed lines show the results of least square fitting over $2.5 < \log_{10} t < 3.5$. Some of the slope values cited in the text are indicated.

aspects are consistent with the apparent multifractality caused by regime behavior described in the previous section. Second, we calculate $h(q)$ over a range of longer time scales $3.2 < \log_{10} t < 4.2$ (i.e. $1585 < t < 15848$ year) although the scaling laws are not so clear in this range. The resulting generalized Hurst exponents $h(q)$ are monotonically decreasing as shown in Figs. 8(c) and 8(d), which confirms the calculations of Shao and Ditlevsen (2016).

Figures 9 and 10 compare the generalized fluctuation functions $F_q(t/\Delta t)$ of the data with those simulated by the SDS model. We obtain good agreements for large positive q. The agreements are worse for $q < 0$ because the calibrated model is too oscillatory in comparison with the data before 71 kyr b2k, and fail to reproduce the long interstadials before 71 kyr b2k. These shortcomings were previously discussed in Mitsui and Crucifix (2017). Despite the discrepancy in $F_q(t/\Delta t)$, the generalized Hurst exponents $h(q)$ are qualitatively well reproduced by the SDS model, as shown in Fig. 8.

4.4 Power spectral analysis of DO signals

We now revisit the nature of spectral scaling exponents mentioned in Section 1. We have obtained the spectral scaling exponent over the frequency range $-3.5 < \log_{10} f < -2.5$ as follows: $\beta = 1.78 \pm 0.04$ for $\log_{10}[\mathrm{Ca}^{2+}]$ and $\beta = 1.41 \pm 0.03$ for δ^{18}O (Figs. 2). These values are fully consistent with those of the generalized Hurst exponent $h(2)$ over $2.5 < \log_{10} t < 3.5$ via Eq. (3): $h(2) = 1.40 \pm 0.05$ for $\log_{10}[\mathrm{Ca}^{2+}]$ and $h(2) = 1.19 \pm 0.01$ for δ^{18}O. As discussed in the previous subsection, the DO signals are apparently multifractal in the time scale $2.5 < \log_{10} t < 3.5$ because of regime behavior. Hence, the corresponding spectral scalings may also be seen as the signature of regime behavior.

The power spectral densities of DO signals are also well reproduced by the SDS model as shown in Figs. 11(a) and 11(b). The local scaling exponent is also well reproduced by the model as shown in Figs. 11(c) and 11(d). This result suggests that

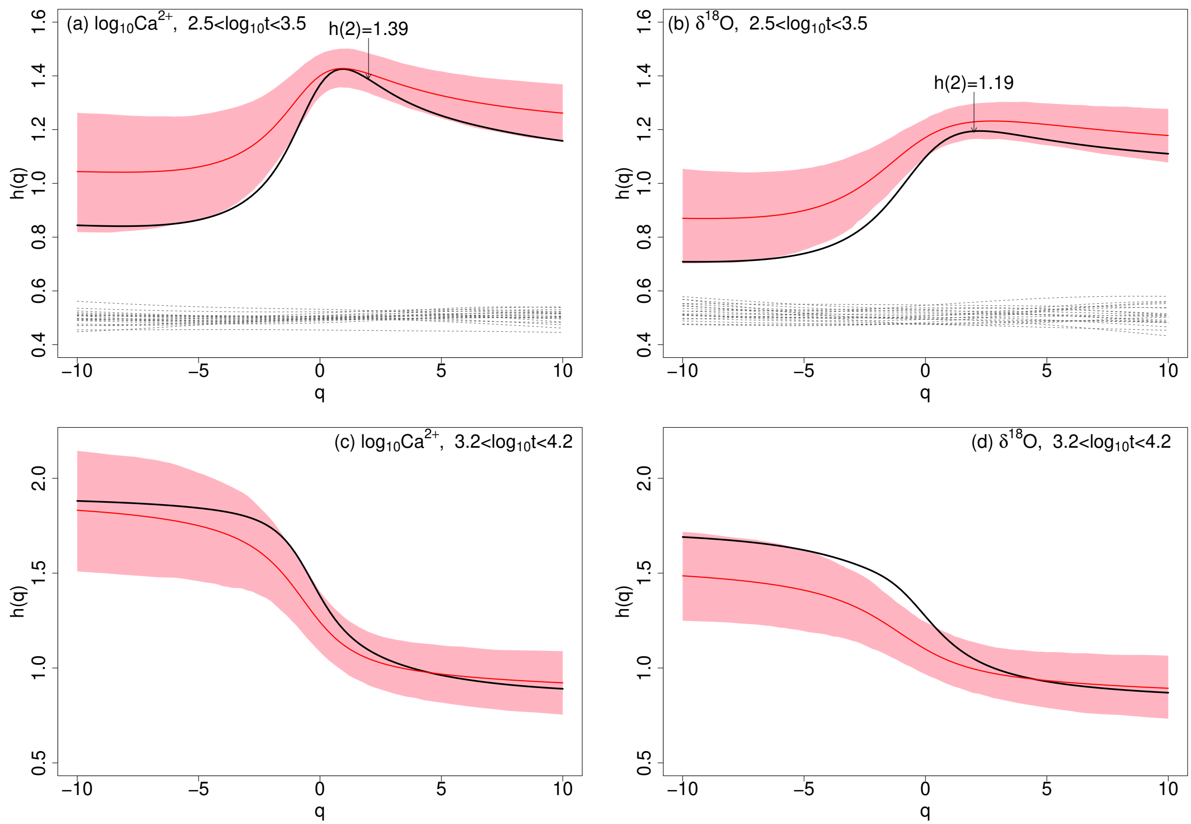

Figure 8. MF-DFA2 generalized Hurst exponent $h(q)$ of Greenland ice core records (black solid line). Each panel also shows the results of simulations with the stochastic dynamical system model: the red line shows the mean of 1000 simulated $h(q)$ with different noise realizations, and the strip shows the 2.5–97.5 percentile range. (a) $h(q)$ of $\log_{10}[\mathrm{Ca}^{2+}]$ obtained by a fitting over a shorter segment range $2.5 < \log_{10} t < 3.5$. The gray dashed lines show the exponents $h(q)$ for 20 randomly shuffled data. (b) $h(q)$ of δ^{18}O obtained by the fitting over a shorter segment range $2.5 < \log_{10} t < 3.5$. (c) $h(q)$ of $\log_{10}[\mathrm{Ca}^{2+}]$ obtained by the fitting over a longer segment range $3.2 < \log_{10} t < 4.2$. (d) $h(q)$ of δ^{18}O obtained by the fitting over a longer segment range $3.2 < \log_{10} t < 4.2$.

the deviations from a scaling law is not a statistical artifact, caused, for example, by lack of data. It as an expected consequence of stochastic regime switches together with highly-deterministic external forcings.

5 Discussion

Shao and Ditlevsen (2016) reported a monotonically decreasing generalized Hurst exponent $h(q)$ for glacial NGRIP δ^{18}O, which is qualitatively similar to Fig. 8(d). This is due to the fact that they calculated the generalized Hurst exponent $h(q)$ over the long time range spanning from $\sim 10^{2.5}$ yr to $\sim 10^{4.5}$ yr (their Fig. 3a), with the MF-DFA1, i.e., with no detrending for the original record. We could reproduce this behaviour by using the MF-DFA1 and the same fitting range as theirs. Thus, our results

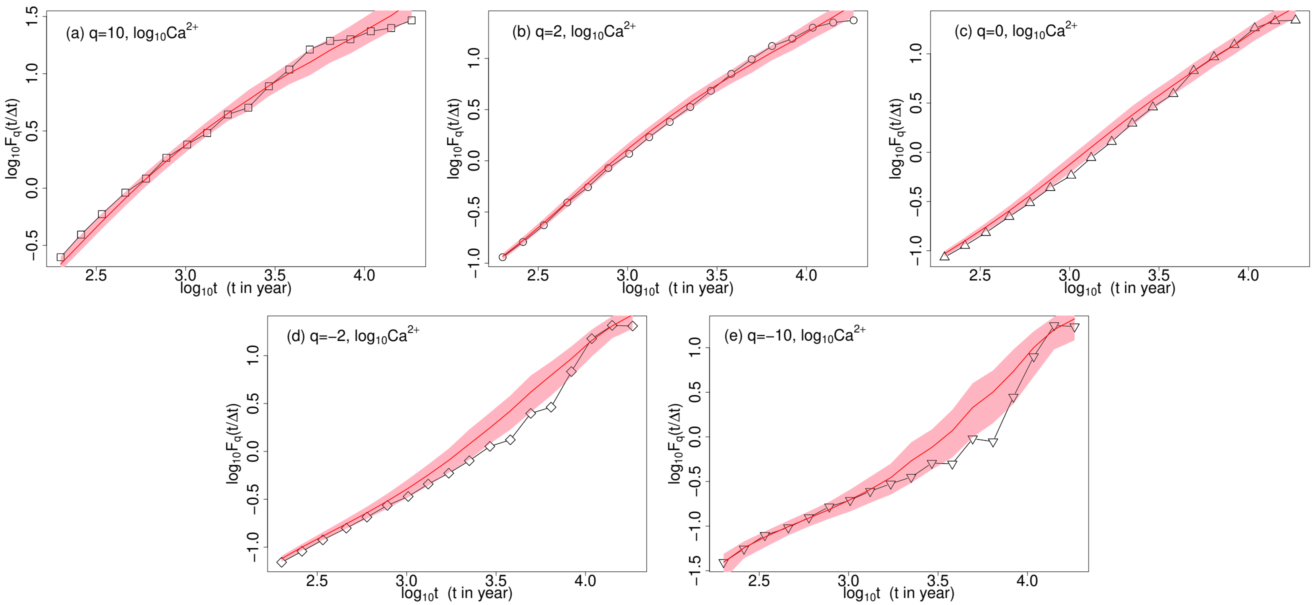

Figure 9. MF-DFA2 generalized fluctuation functions $F_q(t/\Delta t)$ for the NGRIP $\log_{10}[\mathrm{Ca}^{2+}]$ record. Each panel shows the result for a different value of q. The functions $F_q(t/\Delta t)$ for the data are shown by points. The red line shows the mean of 1000 simulated $F_q(t/\Delta t)$ with different noise realizations, and the strip shows the 2.5–97.5 percentile range.

do not contradict those of Shao and Ditlevsen (2016), but we stress that the generalized Hurst exponent $h(q)$ characterizing scaling behavior is changing from unimodal to monotonically decreasing within the time range relevant to DO cycles (Figs. 8). Thus, the most pronounced mode in glacial periods, the DO signal, should not be considered as scale invariant.

Contrary to other works, Rypdal and Rypdal (2016) find evidence for monofractality in NGRIP δ^{18}O record with the wavelet-based multifractal analysis method (see their p. 286 and Fig. 4(k)). In their paper, only positive moments ($q > 0$) are assessed. Our results show that the generalized Hurst exponent $h(q)$ is less dependent on positive q (i.e, closer to monofractal) for NGRIP δ^{18}O (see Figs. 8(b) and 8(d)). Thus, our results are partially in line with their results, but we stress that the $\log_{10}[\mathrm{Ca}^{2+}]$ record presents apparent multifractality even for $q > 0$.

The scaling behavior of the generalized fluctuation functions $F_q(t/\Delta t)$ for $q \ll 0$ changes in $\frac{\tau_{\max}}{2} < t < \tau_{\max}$. The robustness of this property is assessed by changing the length of the dataset so as to give a different value to the maximum duration of a single regime $\tau_{\max}$, as shown in Fig. 12. Thus, we need to be cautious of the fact that the 'statistics' of MF-DFA could be affected by a single event. On the other hand, time series analyses and climate modeling suggest that the duration of a stadial or interstadial is influenced by the changes in background climate conditions (Mitsui and Crucifix, 2017) such as the insolation, the ice volume (McManus et al., 1999; Schulz et al., 2002; Sherriff-Tadano et al., 2018) and the atmospheric CO_2 concentration (Kawamura et al., 2017; Zhang et al., 2017). Thus, the apparent multifractality of DO cycles is determined not only by decadal-to-millennial scale dynamics but also by the 100-kyr glacial cycle.

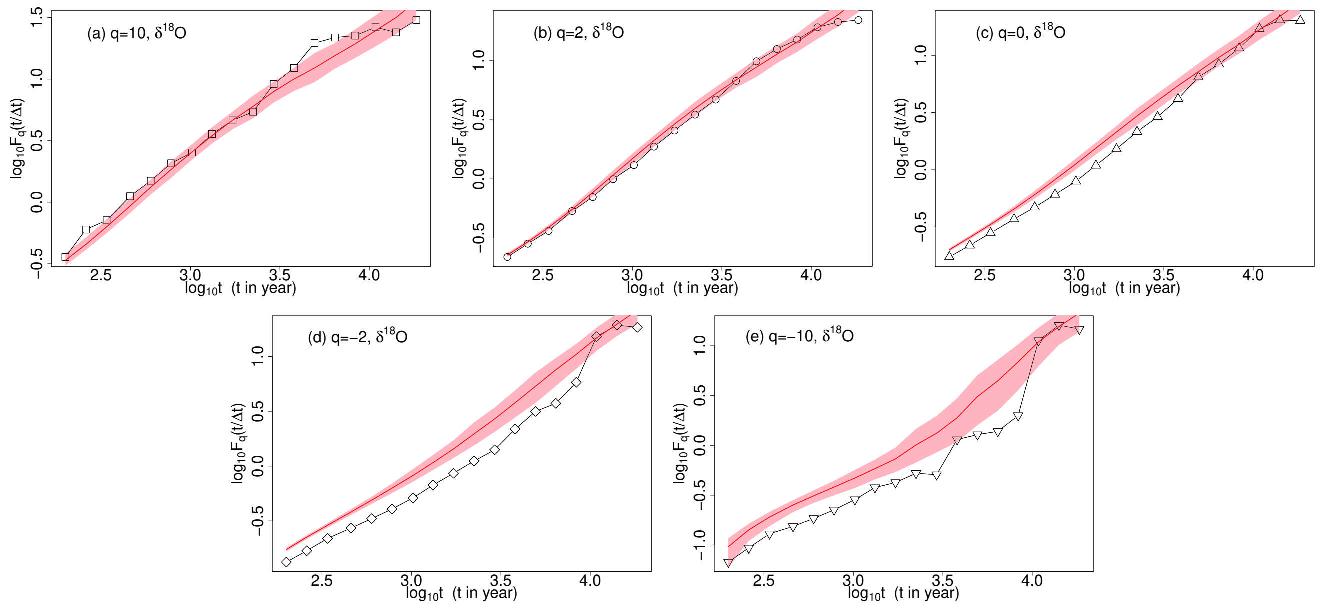

Figure 10. MF-DFA2 Generalized fluctuation functions $F_q(t/\Delta t)$ for the NGRIP δ^{18}O record. Each panel shows the result for a different value of q. The function $F_q(t/\Delta t)$ for the data is shown by points. The red line shows the mean of 1000 simulated $F_q(t/\Delta t)$ with different noise realizations, and the strip shows the 2.5–97.5 percentile range.

The fractional Brownian motion (fBm) with parameter $0 < H < 1$ exhibits the nontrivial scaling $f^{-\beta}$ ($\beta = 2H + 1$) and hence it is sometimes considered as a good time series model of DO signals. However, it is rigorously monofractal and Gaussian, while the records are apparently multifractal as shown here, and they are characterized by non-Gaussian (bimodal) probability density functions (Wunsch, 2003a; Monahan et al., 2008; Mitsui and Crucifix, 2017). In fact, given our present results, fractal process should not necessarily be invoked to explain the properties of DO signal.

Schmitt et al. (1995) suggest that the multifractality of DO events is the manifestation of a multifractal cascade process with intermittency, analogous to turbulent atmospheric temperatures. Since DO cycles are linked to atmospheric, oceanic and cryospheric dynamics, it is indeed not unreasonable to see a possible role of turbulent-like cascade processes in determining the scaling properties. However, the general argument based on cascade processes does not explain why we would find systematic deviations of the local spectral scaling exponent from a power law (Fig. 11). Neither does it explain the change in the generalized Hurst exponent $h(q)$ within the range between multi-centennial and sub-orbital scale (Fig. 8). The simple regime behavior model presented here provides such explanations [4].

There are still discrepancies between the generalized fluctuation function of our model and that of the data for negative q (Figs. 9 and 10). We speculate that some linear stochastic models with Markov-switching (Peavoy and Franzke, 2010;

[4]Similar results have been obtained with slightly different models, for example, a one-dimensional double-well potential model forced by both external forcings and red noise represented by an OU process.

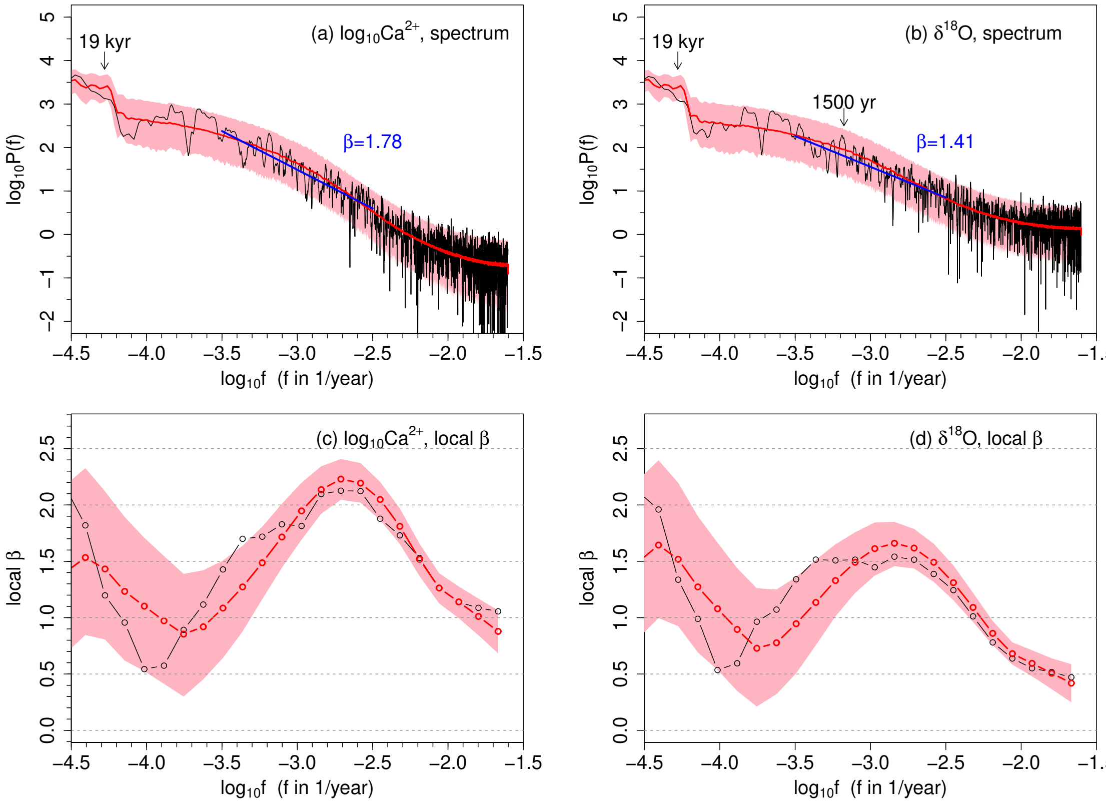

Figure 11. (a) MTM power spectral density (PSD) of NGRIP $\log_{10}[\mathrm{Ca}^{2+}]$ (black line). (b) MTM PSD of NGRIP δ^{18}O (black line). Each panel shows also the result of simulations with the stochastic dynamical system model: the red lines show the mean of 1000 simulated PSDs with different noise realizations, and the strip shows the 2.5–97.5 percentile range. The scaling law over $-3.5 < \log_{10} f < -2.5$ is indicated by the blue line. The bandwidth parameter $NW = 2$ and three tapers are used. The upper left arrow indicates one of the astronomical frequencies, 19 kyr, present in the forcing. (c) The local scaling exponent for NGRIP $\log_{10}[\mathrm{Ca}^{2+}]$ as a function of the center position of the frequency interval over which the exponent is calculated (black circle). The size of the frequency interval for estimating the local β is set to have one order of magnitude. The red line with points shows the mean of the 1000 values of local scaling exponent simulated with the stochastic dynamical system model. The strip shows the 2.5–97.5 percentile range. (d) Same as panel (c) but for NGRIP δ^{18}O.

Kwasniok, 2013) or some elaborated stochastic dynamical system models (Ditlevsen, 1999; Krumscheid et al., 2015; Boers et al., 2017, 2018; Lohmann and Ditlevsen, 2018) may improve the model-data agreement.

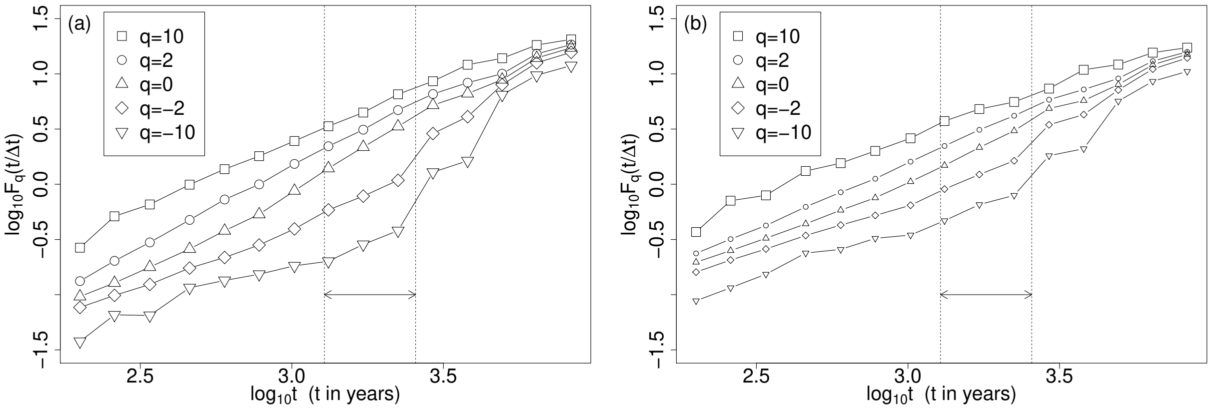

Figure 12. Assessing the sensitivity to $\tau_{\max}$: MF-DFA2 generalized fluctuation functions $F_q(t/\Delta t)$ for (a) NGRIP $\log_{10}$[Ca^{2+}] record and (b) NGRIP δ^{18}O record over 26,000–62,000 years b2k. In this case, the maximum duration of a single regime is $\tau_{\max} = 2,560$ years for 59,440–62,000 years b2k (a late part of GS-28). The functions $F_q(t/\Delta t)$ for the data are shown by different points depending on q. The scaling behavior changes in the range $\frac{\tau_{\max}}{2} < t < \tau_{\max}$ are indicated by the arrows.

6 Conclusions

The Greenland ice core records exhibit nontrivial spectral scaling properties, and this observation was interpreted in various ways by different investigators. This is perhaps a general problem: power spectra of climate records are often said to exhibit power-law scalings, but the cause of the scalings has not been identified unambiguously.

In this work, the cause of the spectral scalings of the glacial climatic fluctuations measured in Greenland ice core records was investigated with multifractal detrended fluctuation analysis. Basing ourselves on three simple models, we documented a form of apparent multifractality that can characterize regime behavior: it has a generalized Hurst exponent $h(q)$ with lower values for $q \ll 0$ than for $q > 0$. This was summarized in Section 3.3. By randomly shuffling the data we confirmed that the multifractality observed in these models is caused by a difference between the autocorrelations of small fluctuations (almost random fluctuations within each regime) and those of large fluctuations (regime shifts). Since the autocorrelation times of these fluctuations are finite, the multifractal character is only apparent. Then, we showed that the observed multifractality of DO signals, reported in previous articles and confirmed here, is in fact a manifestation of that kind of regime-behavior multifractality, observed and characterized with the toy models. Thus, neither the local scaling in the power spectrum nor the apparent multifractality observed for DO cycles necessarily implies that the underlying process is scale-invariant. Indeed, the local value of the scaling exponent β decreases from one-thousand-year scale to ten-thousand-year scale prior to the orbital hump. These changes in the local scaling exponent were also captured by a SDS model forced by insolation and ice volume changes. This result suggests that the deviations from a scaling law is not a statistical artifact, caused, for example, by a lack of data. It is simply caused by stochastic regime switches, and reinforced by the presence of the deterministic external forcings. Our message is that that while the power-laws are undoubtedly useful for obtaining a big picture of climate variability, it would also be important to focus on the more detailed structures of the power spectra, which can be overlooked if the scale-invariance is assumed a priori.

The theory of apparent multifractality of regime behavior described in this work is quite general. Hence, it might be applicable to other types of climatic regime behavior over much shorter time scales (Hannachi et al., 2017) or even to the phenomenon of geomagnetic reversals (Pelletier, 2002) given the well-known similarity between Rikitake two-disk dynamo model of geomagnetic reversals (Rikitake, 1958) and Lorenz (1963) model studied in Appendix C.

Appendix A: Ornstein-Uhlenbeck process and Lorentzian spectrum

The Ornstein-Uhlenbeck (OU) process, $x(t)$, is given by

$$\frac{dx(t)}{dt} = -\lambda x(t) + \xi(t),$$

where λ is the decay rate and $\xi(t)$ represents a white Gaussian noise with variance σ^2. Since it is solved as $x(t) = \int_{-\infty}^{t} e^{-\lambda(t-s)}\xi(s)ds$, its autocovariance is $\langle x(t)x(t+\tau)\rangle = \frac{\sigma^2}{2\lambda}e^{-\lambda|\tau|}$. By the Wiener-Khinchin theorem, the (two-sided) power spectral density (PSD) is given as the Fourier transform of the autocovariance:

$$P(f) = \int_{-\infty}^{\infty} \langle x(t)x(t+\tau)\rangle e^{-2\pi i f\tau} d\tau = \frac{\sigma^2}{\lambda^2 + (2\pi f)^2},$$

which is a Lorentzian. This PSD scales as $P(f) \sim f^{-2}$ for $f \gg \lambda/(2\pi)$ and $P(f) \sim$ const. for $f \ll \lambda/(2\pi)$.

Appendix B: Spectrum of the Stommel-Cessi model

As discussed in Section 3.2, the power spectral density (PSD) of the Stommel-Cessi model can be approximated by the sum of three PSDs $P(f) = P_1(f) + P_2(f) + P_3(f)$: one is a Lorentzian PSD $P_1(f)$ corresponding to random telegraphic jumps between potential minima, and the other two PSDs, $P_2(f)$ and $P_3(f)$, corresponding to linearized equations around each minimum (OU processes), respectively.

First, we derive $P_1(f)$ corresponding to random telegraphic jumps. The mean escape time $\langle t_{a\to c}\rangle$ from a potential minimum at y_a to the other one at y_c and the mean escape time $\langle t_{c\to a}\rangle$ are approximately given by

$$\langle t_{a\to c}\rangle \approx \frac{2}{\sigma^2}\int_{y_a}^{y_c} e^{\frac{2V(y)}{\sigma^2}} dy \int_{-\infty}^{y_b} e^{-\frac{2V(z)}{\sigma^2}} dz,$$

$$\langle t_{c\to a}\rangle \approx \frac{2}{\sigma^2}\int_{y_a}^{y_c} e^{\frac{2V(y)}{\sigma^2}} dy \int_{y_b}^{\infty} e^{-\frac{2V(z)}{\sigma^2}} dz.$$

Laplace's method may be used to calculate these integrals, but direct numerical integrations give more accurate values $\langle t_{a\to c}\rangle \approx 151.9$ and $\langle t_{c\to a}\rangle \approx 46.45$. The transition rate from the left well and that from the right well are given by $\langle t_{a\to c}\rangle^{-1}$ and $\langle t_{c\to a}\rangle^{-1}$. Therefore, the PSD $P_1(f)$ is obtained by taking $a = y_a$, $c = y_c$, $\lambda = \langle t_{a\to c}\rangle^{-1}$ and $\mu = \langle t_{c\to a}\rangle^{-1}$ in Eq. (4).

Second, the PSDs $P_2(f)$ and $P_3(f)$ corresponding to the local relaxation processes are derived. Near the minimum at y_a, the dynamics may be approximated by the OU process:

$$\frac{dy}{dt} = -V_{yy}(y_a)(y - y_a) + p'(t), \tag{B1}$$

where $V_{yy}(y)$ is the second derivative of the potential function $V(y)$. The case near the minimum at y_c is discussed just by changing the suffix from a to c. We consider the PSD for discrete-time observations $y(n)$ at integer times $n = 1, 2, ...$ By integrating the system from time n to $n+1$, we obtain the auto-regressive process of order 1 (AR(1))

$$y(n+1) = \alpha_a y(n) + \xi_a(n),$$

where $\alpha_a = e^{-V_{yy}(y_a)}$ and $\xi_a(n)$ is the white Gaussian noise with mean zero and variance $\Delta_a^2 = \frac{\sigma^2(1-\alpha_a^2)}{2V_{yy}(y_a)}$. Thus, the PSD of $y(n)$ is given as that of the AR(1) process: $\Delta_a^2/(1 - 2\alpha_a \cos(2\pi f) + \alpha_a^2)$ (Priestley, 1981). Since the dynamics given by Eq. (B1) contribute to the total power only when the state $y(t)$ is in the potential well with the minimum y_a, the PSD is given as

$$P_2(f) = \frac{\langle t_{a\to c}\rangle}{\langle t_{a\to c}\rangle + \langle t_{c\to a}\rangle} \frac{\Delta_a^2}{1 - 2\alpha_a \cos(2\pi f) + \alpha_a^2}. \tag{B2}$$

The PSD $P_3(f)$ is given by replacing the suffix a by c in Eq. (B2).

Appendix C: Lorenz model

Another example showing regime behavior is the Lorenz (1963) model given by $\frac{dx}{dt} = \sigma(y-x)$, $\frac{dy}{dt} = x(r-z)-y$, $\frac{dz}{dt} = xy - bz$. We use the canonical values of parameters $\sigma = 10$, $r = 28$, and $b = 8/3$ that generate the chaotic attractor resembling a butterfly. The trajectory of variable x visits positive and negative regions in an irregular manner as shown in Fig. A1(a). In this sample trajectory, the maximum dwell time in either region is 8.65, found around $t = 40$. In what follows, we use discrete-time signal $x_n = x(n\Delta t)$ sampled with a time interval $\Delta t = 0.05$. The power spectral density (PSD) of $x(t)$ is shown in Fig. A1(b). In the low frequency region $f < 0.05$ ($\log_{10} f < -1.3$), the PSD is flat, i.e., $\beta = 0$ as in the Lorentzian spectrum (Aizawa, 1982). In the intermediate range of frequency around $0.06 < f < 1$ ($-1.22 < \log_{10} f < 0$), we observe that the PSD approximately scales as $f^{-1/2}$, as reported by Aizawa (1982). In the much higher frequency region, the PSD decays exponentially (e.g., Franzke et al. (2015)).

We first show the results of MF-DFA2, and mention next the dependence on the order of the detrending, m. Figure A1(c) presents the log-log plot of the generalized fluctuation function $F_q(t/\Delta t)$ for $x(t)$, which is transformed from $F_q(s)$ on the discrete time s via $t = s\Delta t$. The triangles present $F_2(t/\Delta t)$ corresponding to the conventional DFA2. The generalized Hurst exponent $h(q)$ for $q = 2$ is close to 0.5 for large t, which is consistent with the spectral scaling exponent $\beta = 0$ in the low frequency region, via the scaling relation $\beta = 2h(2) - 1$.

As in the case of random telegraph process, the maximum dwell time $\tau_{\max} = 8.65$ ($\log_{10} \tau_{\max} = 0.94$) is important. For $t < \tau_{\max}$, the behavior of the generalized fluctuation function $F_q(t/\Delta t)$ largely depends on q (Fig. A1(c)). We assume the existence

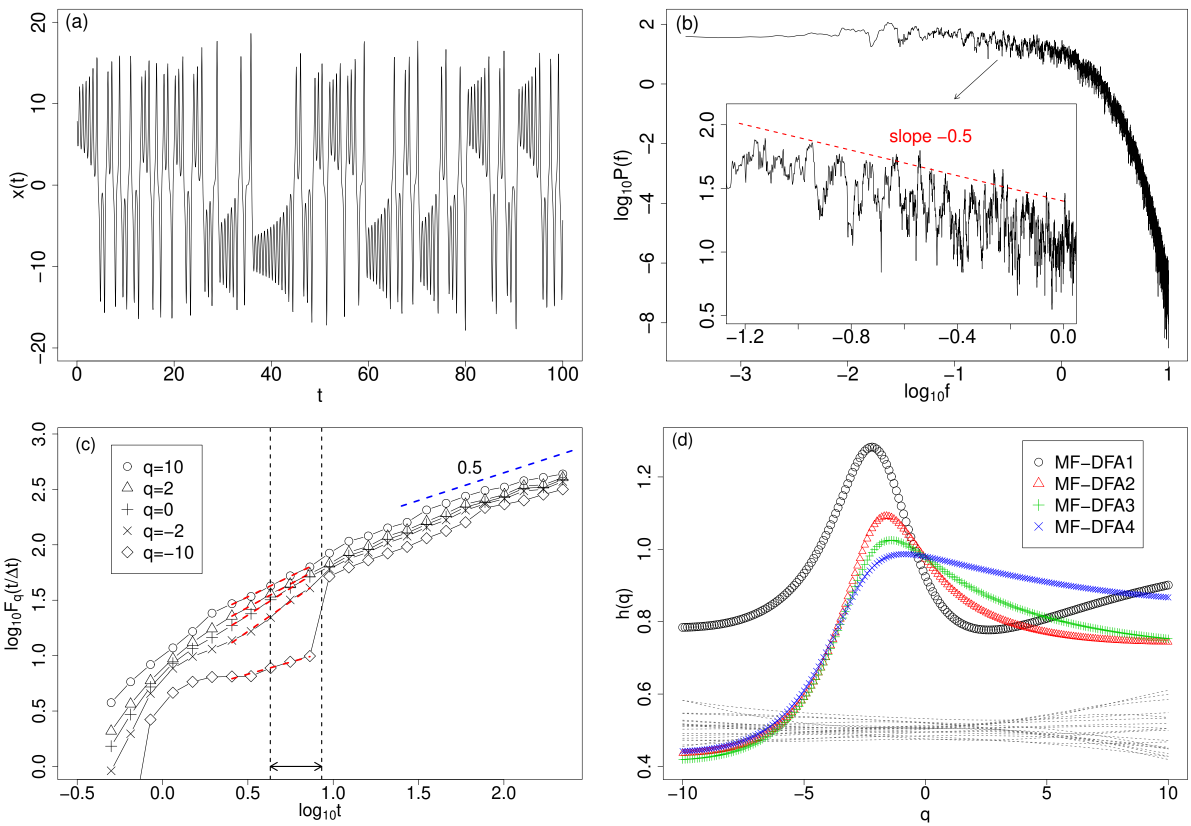

Figure A1. Analysis of Lorenz model. (a) A sample time series of $x(t)$ of Lorenz model observed at $t = s\Delta t$ ($s = 1, 2, \ldots$; $\Delta t = 0.05$). The period $0 \le t \le 100$ is shown. (b) MTM power spectral density of $x(t)$ sampled at $t = s\Delta t$ ($s = 1, 2, \ldots, 20000$; $\Delta t = 0.05$). The inset is a blow-up of a local scaling regime over $0.06 < f < 1$ ($-1.22 < \log_{10} f < 0$). The bandwidth parameter is $NW = 4$, and the number of tapers is $K = 7$. (c) MF-DFA2 generalized fluctuation function $F_q(t/\Delta t)$ for $x(t)$ sampled at $t = s\Delta t$ ($s = 1, 2, \ldots, 20000$; $\Delta t = 0.05$). The scaling behavior changes drastically in the range $\frac{\tau_{\max}}{2} < t < \tau_{\max}$ indicated by the arrow, $\tau_{\max} = 8.56$ is the maximum duration of a single regime, which appears around $t = 40$ in panel (a). (d) Generalized Hurst exponent $h(q)$ obtained by the fitting over $0.4 < \log_{10} t < 0.9$. Each symbol corresponds to a different order of detrending, m, in the MF-DFAm.

of a local multifractal scaling law $F_q(t/\Delta t) \sim t^{h(q)}$ over $0.4 < \log_{10} t < 0.9$ although this is too narrow to be considered as a scaling range. The generalized Hurst exponent $h(q)$ is then obtained as shown in Fig. A1(d). For MF-DFAm ($m \ge 2$), the generalized Hurst exponent $h(q)$ obtained over $0.4 < \log_{10} t < 0.9$ has smaller values for $q \ll 0$ than for $q > 0$.

For $t > \tau_{\max}$, most of the segments in MF-DFAm tend to contain a number of regime transitions. Hence, the contrast between segments with and without regime shifts, which induced q-dependence for $t \lesssim \tau_{\max}$, does not exist. Therefore, it is reasonable to have $h(q) = h(2) = 0.5$.

Acknowledgements. Acknowledgments. We thank Peter Ditlevsen, Wing-Le Chan and two anonymous reviewers for their helpful comments. This work is supported by the Belgian Federal Science Policy Office under contract BR/12/A2/STOCHCLIM. MC is senior research scientist with the Belgian National Fund of Scientific Research. TM is supported by JSPS KAKENHI Grant Number 17H06104. GL is supported by the FSR-FNRS grant PDR T.1056.15 (HOPES).

References

Aizawa, Y.: Global Aspects of the Dissipative Dynamical Systems. I: —Statistical Identification and Fractal Properties of the Lorenz Chaos—, Progress of Theoretical Physics, 68, 64–84, 1982.

Ashkenazy, Y., Baker, D. R., Gildor, H., and Havlin, S.: Nonlinearity and multifractality of climate change in the past 420,000 years, Geophysical research letters, 30, 2003.

Barbante, C., Barnola, J.-M., Becagli, S., Beer, J., Bigler, M., Boutron, C., Blunier, T., Castellano, E., Cattani, O., Chappellaz, J., et al.: One-to-one coupling of glacial climate variability in Greenland and Antarctica, Nature, 444, 195–198, 2006.

Boers, N., Chekroun, M. D., Liu, H., Kondrashov, D., Rousseau, D.-D., Svensson, A., Bigler, M., and Ghil, M.: Inverse stochastic–dynamic models for high-resolution Greenland ice core records, Earth System Dynamics, 8, 1171, 2017.

Boers, N., Ghil, M., and Rousseau, D.-D.: Ocean circulation, ice shelf, and sea ice interactions explain Dansgaard–Oeschger cycles, Proceedings of the National Academy of Sciences, p. 201802573, 2018.

Cessi, P.: A simple box model of stochastically forced thermohaline flow, Journal of Physical Oceanography, 24, 1911–1920, 1994.

Dansgaard, W., Johnsen, S., Clausen, H., Dahl-Jensen, D., Gundestrup, N., Hammer, C., Hvidberg, C., Steffensen, J., Sveinbjörnsdottir, A., Jouzel, J., et al.: Evidence for general instability of past climate from a 250-kyr ice-core record, Nature, 364, 218–220, 1993.

Diebold, F. X. and Inoue, A.: Long memory and regime switching, Journal of econometrics, 105, 131–159, 2001.

Ditlevsen, P. D.: Observation of α-stable noise induced millennial climate changes from an ice-core record, Geophysical Research Letters, 26, 1441–1444, 1999.

Fischer, H., Siggaard-Andersen, M.-L., Ruth, U., Röthlisberger, R., and Wolff, E.: Glacial/interglacial changes in mineral dust and sea-salt records in polar ice cores: Sources, transport, and deposition, Reviews of Geophysics, 45, 2007.

Fraedrich, K. and Blender, R.: Scaling of atmosphere and ocean temperature correlations in observations and climate models, Physical Review Letters, 90, 108 501, 2003.

Fraedrich, K., Blender, R., and Zhu, X.: Continuum climate variability: Long-term memory, scaling, and 1/f-noise, International Journal of Modern Physics B, 23, 5403–5416, 2009.

Frankignoul, C. and Hasselmann, K.: Stochastic climate models, Part II Application to sea-surface temperature anomalies and thermocline variability, Tellus, 29, 289–305, 1977.

Franzke, C. L., Osprey, S. M., Davini, P., and Watkins, N. W.: A dynamical systems explanation of the Hurst effect and atmospheric low-frequency variability, Scientific reports, 5, 2015.

Fredriksen, H.-B. and Rypdal, K.: Spectral characteristics of instrumental and climate model surface temperatures, Journal of Climate, 29, 1253–1268, 2016.

Fredriksen, H.-B. and Rypdal, M.: Long-range persistence in global surface temperatures explained by linear multi-box energy balance models, Journal of Climate, 2017.

Gardiner, C.: Stochastic methods: a handbook for the natural and social sciences 4th ed.(2009), 2009.

Granger, C. W.: Long memory relationships and the aggregation of dynamic models, Journal of econometrics, 14, 227–238, 1980.

Hannachi, A., Straus, D. M., Franzke, C. L., Corti, S., and Woollings, T.: Low Frequency Nonlinearity and Regime Behavior in the Northern Hemisphere Extra-Tropical Atmosphere, Reviews of Geophysics, 2017.

Harris, F. J.: On the use of windows for harmonic analysis with the discrete Fourier transform, Proceedings of the IEEE, 66, 51–83, 1978.

Hasselmann, K.: Stochastic climate models part I. Theory, Tellus, 28, 473–485, 1976.

Heneghan, C. and McDarby, G.: Establishing the relation between detrended fluctuation analysis and power spectral density analysis for stochastic processes, Physical review E, 62, 6103, 2000.

Höll, M. and Kantz, H.: The fluctuation function of the detrended fluctuation analysis—investigation on the AR (1) process, The European Physical Journal B, 88, 126, 2015.

Huybers, P. and Curry, W.: Links between annual, Milankovitch and continuum temperature variability, Nature, 441, 329, 2006.

Kantelhardt, J. W.: Fractal and multifractal time series, in: Encyclopedia of Complexity and Systems Science, pp. 3754–3779, Springer, 2009.

Kantelhardt, J. W., Zschiegner, S. A., Koscielny-Bunde, E., Havlin, S., Bunde, A., and Stanley, H. E.: Multifractal detrended fluctuation analysis of nonstationary time series, Physica A: Statistical Mechanics and its Applications, 316, 87–114, 2002.

Kantelhardt, J. W., Koscielny-Bunde, E., Rybski, D., Braun, P., Bunde, A., and Havlin, S.: Long-term persistence and multifractality of precipitation and river runoff records, Journal of Geophysical Research: Atmospheres, 111, 2006.

Kawamura, K., Abe-Ouchi, A., Motoyama, H., Ageta, Y., Aoki, S., Azuma, N., Fujii, Y., Fujita, K., Fujita, S., Fukui, K., et al.: State dependence of climatic instability over the past 720,000 years from Antarctic ice cores and climate modeling, Science advances, 3, e1600 446, 2017.

Klemeš, V.: The Hurst phenomenon: A puzzle?, Water Resources Research, 10, 675–688, 1974.

Kominz, M. A. and Pisias, N. G.: Pleistocene climate: deterministic or stochastic?, Science, 204, 171–173, 1979.

Koscielny-Bunde, E., Bunde, A., Havlin, S., Roman, H. E., Goldreich, Y., and Schellnhuber, H.-J.: Indication of a universal persistence law governing atmospheric variability, Physical Review Letters, 81, 729, 1998.

Koscielny-Bunde, E., Kantelhardt, J. W., Braun, P., Bunde, A., and Havlin, S.: Long-term persistence and multifractality of river runoff records: Detrended fluctuation studies, Journal of Hydrology, 322, 120–137, 2006.

Krumscheid, S., Pradas, M., Pavliotis, G., and Kalliadasis, S.: Data-driven coarse graining in action: Modeling and prediction of complex systems, Physical Review E, 92, 042 139, 2015.

Kwasniok, F.: Analysis and modelling of glacial climate transitions using simple dynamical systems, Philosophical Transactions of the Royal Society of London A: Mathematical, Physical and Engineering Sciences, 371, 20110 472, 2013.

Laskar, J., Robutel, P., Joutel, F., Gastineau, M., Correia, A., and Levrard, B.: A long-term numerical solution for the insolation quantities of the Earth, Astronomy & Astrophysics, 428, 261–285, 2004.

Lisiecki, L. E. and Raymo, M. E.: A Pliocene-Pleistocene stack of 57 globally distributed benthic δ18O records, Paleoceanography, 20, 2005.

Lohmann, J. and Ditlevsen, P. D.: A consistent statistical model selection for abrupt glacial climate changes, Climate Dynamics, pp. 1–16, 2018.

Lorenz, E. N.: Deterministic nonperiodic flow, Journal of the atmospheric sciences, 20, 130–141, 1963.

Lovejoy, S.: A voyage through scales, a missing quadrillion and why the climate is not what you expect, Climate Dynamics, 44, 3187–3210, 2015.

Lovejoy, S. and Schertzer, D.: Haar wavelets, fluctuations and structure functions: convenient choices for geophysics, Nonlinear Processes in Geophysics, 19, 513–527, 2012.

Lovejoy, S. and Schertzer, D.: The weather and climate: emergent laws and multifractal cascades, Cambridge University Press, 2013.

Ludescher, J., Bogachev, M. I., Kantelhardt, J. W., Schumann, A. Y., and Bunde, A.: On spurious and corrupted multifractality: The effects of additive noise, short-term memory and periodic trends, Physica A: Statistical Mechanics and its Applications, 390, 2480–2490, 2011.

Mandelbrot, B. B. and Van Ness, J. W.: Fractional Brownian motions, fractional noises and applications, SIAM review, 10, 422–437, 1968.

Markonis, Y. and Koutsoyiannis, D.: Climatic variability over time scales spanning nine orders of magnitude: Connecting Milankovitch cycles with Hurst–Kolmogorov dynamics, Surveys in Geophysics, 34, 181–207, 2013.

Marsh, N. D. and Ditlevsen, P. D.: Observation of atmospheric and climate dynamics from a high resolution ice core record of a passive tracer over the last glaciation, Journal of Geophysical Research: Atmospheres, 102, 11 219–11 224, 1997.

Mayewski, P. A., Meeker, L. D., Twickler, M. S., Whitlow, S., Yang, Q., Lyons, W. B., and Prentice, M.: Major Features and Forcing of High-atitude Northern Hemisphere Atmospheric Circulation using a 110,000-year-long Glaciochemical Series, Journal of Geophysical Research—Oceans, 102, 26–345, 1997.

McManus, J. F., Oppo, D. W., and Cullen, J. L.: A 0.5-million-year record of millennial-scale climate variability in the North Atlantic, Science, 283, 971–975, 1999.

Mitsui, T. and Crucifix, M.: Influence of external forcings on abrupt millennial-scale climate changes: a statistical modelling study, Climate Dynamics, 48, 2729–2749, 2017.

Monahan, A. H., Alexander, J., and Weaver, A. J.: Stochastic models of the meridional overturning circulation: time scales and patterns of variability, Philosophical Transactions of the Royal Society of London A: Mathematical, Physical and Engineering Sciences, 366, 2525–2542, 2008.

Nilsen, T., Rypdal, K., and Fredriksen, H.: Long-range memory in temperature reconstructions from ice cores; glacial vs interglacial climate conditions, in: AGU Fall Meeting Abstracts, 2014.

Nilsen, T., Rypdal, K., and Fredriksen, H.-B.: Are there multiple scaling regimes in Holocene temperature records?, Earth System Dynamics, 7, 419–439, 2016.

Paillard, D.: The timing of Pleistocene glaciations from a simple multiple-state climate model, Nature, 391, 378–381, 1998.

Peavoy, D. and Franzke, C.: Bayesian analysis of rapid climate change during the last glacial using Greenland δ 18 O data, Climate of the Past, 6, 787–794, 2010.

Pelletier, J. D.: The power spectral density of atmospheric temperature from time scales of 10- 2 to 106 yr, Earth and planetary science letters, 158, 157–164, 1998.

Pelletier, J. D.: Natural variability of atmospheric temperatures and geomagnetic intensity over a wide range of time scales, Proceedings of the National Academy of Sciences, 99, 2546–2553, 2002.

Pelletier, J. D. and Turcotte, D. L.: Self-affine time series: II. Applications and models, Advances in Geophysics, 40, 91–166, 1999.

Peng, C.-K., Buldyrev, S. V., Havlin, S., Simons, M., Stanley, H. E., and Goldberger, A. L.: Mosaic organization of DNA nucleotides, Physical review e, 49, 1685, 1994.

Potter, K. W.: Evidence for nonstationarity as a physical explanation of the Hurst phenomenon, Water Resources Research, 12, 1047–1052, 1976.

Priestley, M. B.: Spectral analysis and time series, 1981.

Rahim, K. and Burr, W.: multitaper: Multitaper Spectral Analysis, R package version, pp. 1–0, 2013.

Rahmstorf, S.: Ocean circulation and climate during the past 120,000 years, Nature, 419, 207–214, 2002.

Rasmussen, S. O., Bigler, M., Blockley, S. P., Blunier, T., Buchardt, S. L., Clausen, H. B., Cvijanovic, I., Dahl-Jensen, D., Johnsen, S. J., Fischer, H., et al.: A stratigraphic framework for abrupt climatic changes during the Last Glacial period based on three synchronized Greenland ice-core records: refining and extending the INTIMATE event stratigraphy, Quaternary Science Reviews, 106, 14–28, 2014.

Rhines, A. and Huybers, P.: Estimation of spectral power laws in time uncertain series of data with application to the Greenland Ice Sheet Project 2 δ18O record, Journal of Geophysical Research: Atmospheres, 116, 2011.

Rikitake, T.: Oscillations of a system of disk dynamos, in: Mathematical Proceedings of the Cambridge Philosophical Society, vol. 54, pp. 89–105, Cambridge University Press, 1958.

Rybski, D., Bunde, A., Havlin, S., and Von Storch, H.: Long-term persistence in climate and the detection problem, Geophysical Research Letters, 33, 2006.

Rypdal, K. and Rypdal, M. W.: Late Quaternary temperature variability described as abrupt transitions on a 1/f noise background, 2016.

Rypdal, M.: Early-warning signals for the onsets of Greenland interstadials and the Younger Dryas–Preboreal transition, Journal of Climate, 29, 4047–4056, 2016.

Schmitt, F., Lovejoy, S., and Schertzer, D.: Multifractal analysis of the Greenland ice-core project climate data, Geophysical research letters, 22, 1689–1692, 1995.

Schulz, M., Paul, A., and Timmermann, A.: Relaxation oscillators in concert: A framework for climate change at millennial timescales during the late Pleistocene, Geophysical Research Letters, 29, 46–1, 2002.

Seierstad, I. K., Abbott, P. M., Bigler, M., Blunier, T., Bourne, A. J., Brook, E., Buchardt, S. L., Buizert, C., Clausen, H. B., Cook, E., et al.: Consistently dated records from the Greenland GRIP, GISP2 and NGRIP ice cores for the past 104 ka reveal regional millennial-scale δ 18 O gradients with possible Heinrich event imprint, Quaternary Science Reviews, 106, 29–46, 2014.

Shackleton, N. and Imbrie, J.: The δ 18O spectrum of oceanic deep water over a five-decade band, Climatic Change, 16, 217–230, 1990.

Shao, Z.-G. and Ditlevsen, P. D.: Contrasting scaling properties of interglacial and glacial climates, Nature communications, 7, 2016.

Sherriff-Tadano, S., Abe-Ouchi, A., Yoshimori, M., Oka, A., and Chan, W.-L.: Influence of glacial ice sheets on the Atlantic meridional overturning circulation through surface wind change, Climate Dynamics, 50, 2881–2903, 2018.

Stocker, T. F. and Johnsen, S. J.: A minimum thermodynamic model for the bipolar seesaw, Paleoceanography, 18, 2003.

Stommel, H.: Thermohaline convection with two stable regimes of flow, Tellus, 13, 224–230, 1961.

Thomson, D. J.: Spectrum estimation and harmonic analysis, Proceedings of the IEEE, 70, 1055–1096, 1982.

Voelker, A. H. et al.: Global distribution of centennial-scale records for Marine Isotope Stage (MIS) 3: a database, Quaternary Science Reviews, 21, 1185–1212, 2002.

Witt, A. and Malamud, B. D.: Quantification of long-range persistence in geophysical time series: conventional and benchmark-based improvement techniques, Surveys in Geophysics, 34, 541–651, 2013.

Wolff, E. W., Chappellaz, J., Blunier, T., Rasmussen, S. O., and Svensson, A.: Millennial-scale variability during the last glacial: The ice core record, Quaternary Science Reviews, 29, 2828–2838, 2010.

Wunsch, C.: Greenland—Antarctic phase relations and millennial time-scale climate fluctuations in the Greenland ice-cores, Quaternary Science Reviews, 22, 1631–1646, 2003a.

Wunsch, C.: The spectral description of climate change including the 100 ky energy, Climate Dynamics, 20, 353–363, 2003b.

Yiou, R., Fuher, K., Meeker, L., Jouzel, J., Johnsen, S., and Mayewski, P. A.: Paleoclimatic variability inferred from the spectral analysis of Greenland and Antarctic ice-core data, Journal of Geophysical Research—Oceans, 102, 26–441, 1997.

Zhang, X., Knorr, G., Lohmann, G., and Barker, S.: Abrupt North Atlantic circulation changes in response to gradual CO 2 forcing in a glacial climate state, Nature Geoscience, 10, 518, 2017.